DETERMINATION OF THE EFFECTIVE THERMAL CONDUCTIVITY OF PACKED BEDS OF MAGNESIUM-MANGANESE-OXIDE

By

Faezeh Masoomi

A THESIS

Submitted to
Michigan State University
in partial fulfillment of the requirements
for the degree of

Mechanical Engineering – Master of Science

2021

ABSTRACT

DETERMINATION OF THE EFFECTIVE THERMAL CONDUCTIVITY OF PACKED BEDS OF MAGNESIUM-MANGANESE-OXIDE

By

Faezeh Masoomi

Magnesium-manganese-oxide redox materials have significant potential for thermochemical energy storage; however, the material high-temperature physical properties, in particular, its thermal conductivity are critical for engineering storage devices.

In this thesis, the effective thermal conductivity of packed beds of magnesium-manganese-oxide pellets is measured in the temperature range of 300 °C to 1300 °C with a 100 °C span using the transient hot-probe method. The transient hot-probe method is a well-established technique to determine the effective thermal conductivity of materials by measuring the transient temperature response of a 1-D heat source with constant heat generation. In this thesis, a thin platinum wire covered by a thin alumina sheet is used as both 1-D heat source, and the temperature measurement device. A constant current is passed through the platinum wire emulating 1-D heat generation. Simultaneously, the electrical resistance of the wire is measured versus time by measuring the voltage across the platinum wire. The wire temperature is calculated based on the wire's temperature-dependent resistance using a calibration curve established prior to the experiment. The effective thermal conductivity is calculated by curve-fitting a conductivity-dependent model to the wire temperature.

The effective thermal conductivity ranges from 0.46 to 1.64 ($Wm^{-1}K^{-1}$), and increases significantly with the temperature. The increase in thermal conductivity with temperature is primarily attributed to thermal radiation. The experimental results are compared to a theoretical dual-porosity model, showing good agreement.

ACKNOWLEDGEMENTS

First and foremost, I am incredibly grateful to my advisor, Dr. Joerg Petrasch, for his invaluable advice, continuous support, and patience during my master's study. I would also like to thank Dr. Klausner and Dr. Randhir for their supervision and support. I want to thank all my colleagues for their kind help and support which made my study at Michigan State University a wonderful time. Finally, I would like to express my gratitude to my parents. Without their tremendous understanding and encouragement in the past few years, it would be impossible to complete my study.

TABLE OF CONTENTS

LIST OF TABLES

LIST OF FIGURES

KEY TO SYMBOLS AND ABBREVIATIONS

a_w	Coefficient in Woodside and Messmer model
a_1	Coefficient in the calibration formula
a_2	Coefficient in the calibration formula
a_3	Coefficient in the calibration formula
a_4	Coefficient in the calibration formula
A	Coefficient in Equation 3.9
A_i	Coefficient in the polynomial fit of magnesium-oxide thermal conductivity
B	Coefficient in Equation 3.9
B'	scaled coefficient of B
B_i	Coefficient in the polynomial fit of air thermal conductivity
Bi	Biot number
c_w	Coefficient in Woodside and Messmer model
C	Coefficient in Equation 3.9
C_p	Specific heat capacity in constant pressure, $\left(\frac{\mathrm{J}}{\mathrm{kg°C}}\right)$
d	The smallest distance between the probe and the boundary, (m)
d_{pellet}	Manganese-magnesium-oxide pellet diameter, (m)
d_{pore}	Average diameter of pores in the pellet, (m)
d_w	Coefficient in Woodside and Messmer model
D	Coefficient in Equation 3.9
Fo	Fourier number
I	Electrical current, (A)
J_0	Bessel function of the first kind or order zero
J_1	Bessel function of the first kind of order one
k	Thermal conductivity $\left(\frac{\mathrm{W}}{\mathrm{m°C}}\right)$
k_{air}	Air thermal conductivity, $\left(\frac{\mathrm{W}}{\mathrm{m°C}}\right)$
k_{cond}	Conduction component of the effective thermal conductivity, $\left(\frac{\mathrm{W}}{\mathrm{m°C}}\right)$

$k_{\text{cond-bed}}$	Conduction component of the packed bed effective thermal conductivity, $\left(\frac{\text{W}}{\text{m°C}}\right)$
$k_{\text{cond-pellet}}$	Conduction component of the pellet effective thermal conductivity, $\left(\frac{\text{W}}{\text{m°C}}\right)$
k_{eff}	Effective thermal conductivity of packed bed measured in the experiment, $\left(\frac{\text{W}}{\text{m°C}}\right)$
$k_{\text{eff-model}}$	Effective thermal conductivity of packed bed calculated from modeling, $\left(\frac{\text{W}}{\text{m°C}}\right)$
k_{MgO}	Thermal conductivity of magnesium-oxide, $\left(\frac{\text{W}}{\text{m°C}}\right)$
k_{MnO}	Thermal conductivity of manganese-oxide, $\left(\frac{\text{W}}{\text{m°C}}\right)$
k_{MgMnO_2}	Thermal conductivity of magnesium-manganese-oxide without porosity, $\left(\frac{\text{W}}{\text{m°C}}\right)$
k_{pellet}	Effective thermal conductivity of a single pellet, $\left(\frac{\text{W}}{\text{m°C}}\right)$
k_{rad}	Radiation component of the effective thermal conductivity $\left(\frac{\text{W}}{\text{m°C}}\right)$
$k_{\text{rad-bed}}$	Radiation component of the packed bed thermal conductivity $\left(\frac{\text{W}}{\text{m°C}}\right)$
$k_{\text{rad-pellet}}$	Radiation component of the pellet thermal conductivity, $\left(\frac{\text{W}}{\text{m°C}}\right)$
k_{solid}	Thermal conductivity of solid, $\left(\frac{\text{W}}{\text{m°C}}\right)$
K	Coefficient in Zehner and Schlunder model
m	The linear line slope in ΔT_m versus $\ln(t)$ plot
m_{probe}	Mass of the probe (kg)
M	Coefficient in the extinction coefficient
MgO	Magnesium-oxide
MgMnO_2	Magnesium-manganese-oxide
MnO	Manganese-oxide
M_{bed}	Extinction coefficient of the packed bed
M_{pellet}	Extinction coefficient of the pellet
n	Refractive index
N	Coefficient in Zehner and Schlunder model

p	Coefficient in the exponential fit of manganese-oxide
q	Coefficient in the exponential fit of manganese-oxide
Q	Power of 1-D heater per meter, $\left(\frac{\mathrm{W}}{\mathrm{m}}\right)$
r	Radial direction in cylindrical coordinate system
R^2	R-squared
R_c	Contact resistance, $\left(\frac{\mathrm{m}^2}{\mathrm{W°C}}\right)$
R_{shunt}	Electrical resistance of shunt, (Ω)
R_{wire}	Electrical resistance of platinum wire, (Ω)
S_m	Heat capacity of the material, $\left(\frac{\mathrm{J}}{°\mathrm{C}}\right)$
S_s	Heat capacity of the probe, $\left(\frac{\mathrm{J}}{°\mathrm{C}}\right)$
t	Time, (s)
t_0	Initial time, (s)
t_{max}	The upper limit on time in the transient hot-probe method suggested by Vos [2], (s)
t_{min}	The lower limit on time in the transient hot-probe method suggested by Vos [2]. (s)
t_{start}	The lower limit on time based on maximizing R^2, (s)
T	Temperature, (°C)
T_m	Temperature of the heating probe, (°C)
V_{shunt}	The voltage measurement across the shunt, (V)
V_{wire}	The voltage measurement across the platinum wire, (V)
Y_0	Bessel function of the second kind of order zero
Y_1	Bessel function of the second kind of order one
z	z-direction in cylindrical coordinate
α	Thermal diffusivity, $\left(\frac{\mathrm{m}^2}{\mathrm{s}}\right)$
β	Extinction coefficient
β_{bed}	Extinction coefficient of the packed bed

β_{pellet}	Extinction coefficient of the pellet
γ	Euler's constant
σ	Stefan-Boltzman constant
ϕ	Porosity
ϕ_{bed}	Packed bed overall porosity
ϕ_{pellet}	Pellet porosity
Φ	The volume fraction of magnesium-oxide in the magnesium-manganese-oxide mixture
Ω	Inertia contrast

CHAPTER 1

INTRODUCTION

1.1 Energy storage Technologies

Renewable energy resources are a subject of interest worldwide due to their advantages over fossil fuel, the primary energy resource in today's energy market. Renewable energy resources, such as solar, wind, hydro, and biomass, are sustainable and abundant. Unlike fossil fuels, which take millions of years to be formed, renewable resources do not deplete. Renewable energy resources are better for the environment. They have no greenhouse gas emissions, the leading cause of global warming, they also produce less waste, and they do not contaminate the environment. Furthermore, renewable energy resources can bring economic benefits since they have low maintenance costs and can generate electricity locally, lowering the electricity transfer costs, especially for remote areas. Despite these advantages, renewable energies have difficulties finding their potential role in today's energy market. One of the drawbacks is the unpredictable nature of renewable energy resources like solar and wind. The uncertainty associated with these resources requires higher electrical grid flexibility, causing an increase in electricity prices. Electrical Storage Units (ESU) can be a solution to this problem. They can store energy when renewable energy resource is available and release it to the electrical grid when demand is high. Some of these technologies are introduced in Table 1.1.

Table 1.1 summarizes relevant technologies for energy storage. Thermochemical storage is one of the existing technologies for renewable energy storage. It uses reversible chemical reactions to store thermal energy in the form of chemical compounds. In recent years many reactor concepts and materials have been introduced to design a thermochemical unit [3, 4].

Randhir et al. [5] introduced magnesium-manganese-oxide as a promising material to be used in thermochemical storage applications. Magnesium-manganese-oxide is a low-cost, abundant, non-toxic material that uses air as the reacting gas, eliminating the need for a gas storage system.

Pumped storage hydropower (PSH)	Water is being pumped to a reservoir at a higher level during off-peak. The energy is stored in the form of potential energy and can be released by allowing the water to flow back to the lower reservoir and rotating a turbine during peak time.
Compressed air energy storage (CAES)	During peak-off, the air is compressed into the tanks using a rotary compressor. The compressed air can be released to a gas turbine to generate electricity from high-pressure air during peak time.
Batteries	Batteries use chemical reactions to store and release energy. Batteries can be used in distribution, off-grid, and short-term storage.
Thermochemical storage	It uses a reversible chemical reaction to store energy. The reversible chemical reaction can occur in high or low temperatures based on the nature of the chemical reaction.
Chemical hydrogen storage	It uses hydrogen as the energy carrier to store electricity, for example, through electrolysis.
Flywheels	Mechanical devices that store electricity in the form of rotational energy. Slowing down these devices can provide bursts of energy to the electrical grid.
Supercapacitors	Energy is stored in the form of electrostatic between two conductive plates. This technology is used for short terms, producing a short burst of power.
Superconducting magnetic energy storage (SMES)	In this technology, electricity is stored in a magnetic field with a direct current going into a super-conducting coil. The resistance of superconducting material is almost zero, so the energy can be stored for a long time.

Table 1.1: Existing technologies for energy storage

This material stores energy by undergoing a reversible chemical reaction at higher temperatures as follows:

$$\mathrm{MgMnO}_{2+C_1} \Rightarrow \mathrm{MgMnO}_{2+C_2} + \frac{C_1 - C_2}{2}\mathrm{O}_2 \tag{1.1}$$

In which C_1 and C_2 denote the excess oxygen in the material.

Randhir et al. [5] investigated the reactive stability of magnesium-manganese-oxide at high temperatures ($1000 < T < 1500$ °C) for three different molar ratios (Mn/Mg = 2/3, 1/1, and 2/1), and shown than the material's released and absorbed oxygen remains unchanged over 20 cycles, cycling between 1200 and 1500 °C with an oxygen partial pressure of 0.2 atm. Based on these results,

they concluded this material has excellent reactivity stability at higher temperatures. They also measured the energy density of the material in temperatures 1000 to 1500 °C using a combination of acid-solution calorimetry and drop calorimetry. They obtained the volumetric energy density (chemical, phase change, and sensible) of Mn/Mg, for 2/3, 1/1, and 2/1 molar ratios cycles 1596, 1626, and 1654 $\left(\frac{\text{MJ}}{\text{m}^3}\right)$, respectively.

King et al. [6] investigated different methods to enhance thermochemical energy storage density of magnesium-manganese-oxide. They varied the manganese to magnesium molar ratios, and they found that the maximum energy density is at the 1/1 molar ratio. They also observed lowering the oxygen partial pressure below atmospheric during thermal reduction enhances the thermochemical energy storage density.

However, to design a thermochemical storage unit, the magnesium-manganese-oxide's thermophysical properties need to be investigated. Randhir et al. [7] determined the oxidation kinetics of porous magnesium-manganese-oxide pellets at high temperatures. The current thesis investigates the effective thermal conductivity of a packed bed of magnesium-manganese oxide pellets. In the following sections, different measurement techniques will be briefly introduced.

1.2 Thermal conductivity measurement techniques

Experimental approaches for measuring the effective thermal conductivity fall into two general categories: transient and steady-state [8]. In the following sections these methods will be discussed.

1.2.1 Steady state methods

In this category of methods, a heat source in contact with the sample affects a temperature gradient within the material at steady-state condition; the thermal conductivity can be calculated based on the Fourier law.

The steady-state methods are analytically simple. However, there are significant drawbacks to these methods. Achieving high accuracies with steady-state methods is challenging and requires rather

complex experimental setup due to temperature sensor uncertainties and parasitic heat loss [9]. Also, The long wait time to develop the steady-state condition makes it a less appealing candidate for experiments with multiple measurements.

1.2.2 Transient Methods

The transient methods use temperature gradients generated by short-time heating of a 1-D heat source embedded inside the medium to measure the effective thermal conductivity. The transient methods fall into different categories based on various contact forms, for example, transient hot strip, transient hot plane, or transient hot disk. The transient methods are used extensively due to simplicity and the short wait time [8, 10, 11]. These methods have been proven to be the best for investigating the thermal conductivity of liquids and gases. However, it has been popular with solids as well, for example, in applications like geometrical features [12], nuclear pebble beds [13],and porous materials [14].

The commercial hot probe, an instrument for in situ measurements, is designed based on the transient hot-wire method. However, recent works put more limitations on transient probe methods. A study at the University of Plymouth has shown that commercial thermal probe measurements can only be reliable for materials with thermal conductivity above $0.07 \left(\frac{W}{m^{\circ}C}\right)$ [15].

Based on the simplified analytical solution of the heat conduction equation, the temperature of a 1-D heat source with constant heat generation must increase linearly with logarithmic time after a short period. The thermal conductivity of the material is calculated based on the slope of this linear function. However, this curve can deviate from the linear shape due to boundary conditions, inhomogeneity, or moisture content. Marmoret et al. [16] demonstrated that estimating the effective thermal conductivity from the slope of the sigmoid curve will result in inaccurate estimations.

CHAPTER 2

MATHEMATICAL MODELING

2.1 Introduction

Different models have been introduced to estimate the effective thermal conductivity of porous media [17]. These models are introduced based on various parameters, such as porosity, texture, and porous structure. Different modes of heat transfer can contribute to the effective thermal conductivity of porous materials. For high-temperature applications, radiation will play a significant role in the effective thermal conductivity and needs to be considered in the modeling. For our application, the overall effective thermal conductivity is assumed to have two major contributing factors: conduction and radiation. The summation of these two components will make up the total effective thermal conductivity.

$$k_{\text{eff}-\text{model}} = k_{\text{cond}} + k_{\text{rad}} \tag{2.1}$$

Multiple models need to be used at different modeling stages to accurately estimate the effective thermal conductivity of the packed bed of magnesium-manganese-oxide pellets. As a well-accepted approximation, a packed bed of pellets can be considered as a 1-D homogeneous porous system [18]. Still, the magnesium-manganese-oxides pellets have an internal porous structure, so their conductivity needs to be calculated prior to the packed bed. Also, since there is no experimental data, the bulk material thermal conductivity of magnesium-manganese-oxide needs to be estimated from its components. The bulk material thermal conductivity can be modeled using a dual-porosity model [19], and a mixing rule as follows:

Step 1: Calculating the thermal conductivity of magnesium-manganese-oxide based on its components, magnesium-oxide and manganese-oxide via a mixing rule.

Step 2: Calculating the effective thermal conductivity of a single pellet, considering the pellet porosity and manganese-magnesium-oxide thermal conductivity from step 1, as the small scale.

Step 3: Calculating the effective thermal conductivity of the packed bed of magnesium-manganese-oxide pellets, considering the bed porosity and the effective thermal conductivity of a single pellet from step 2, as the large scale.

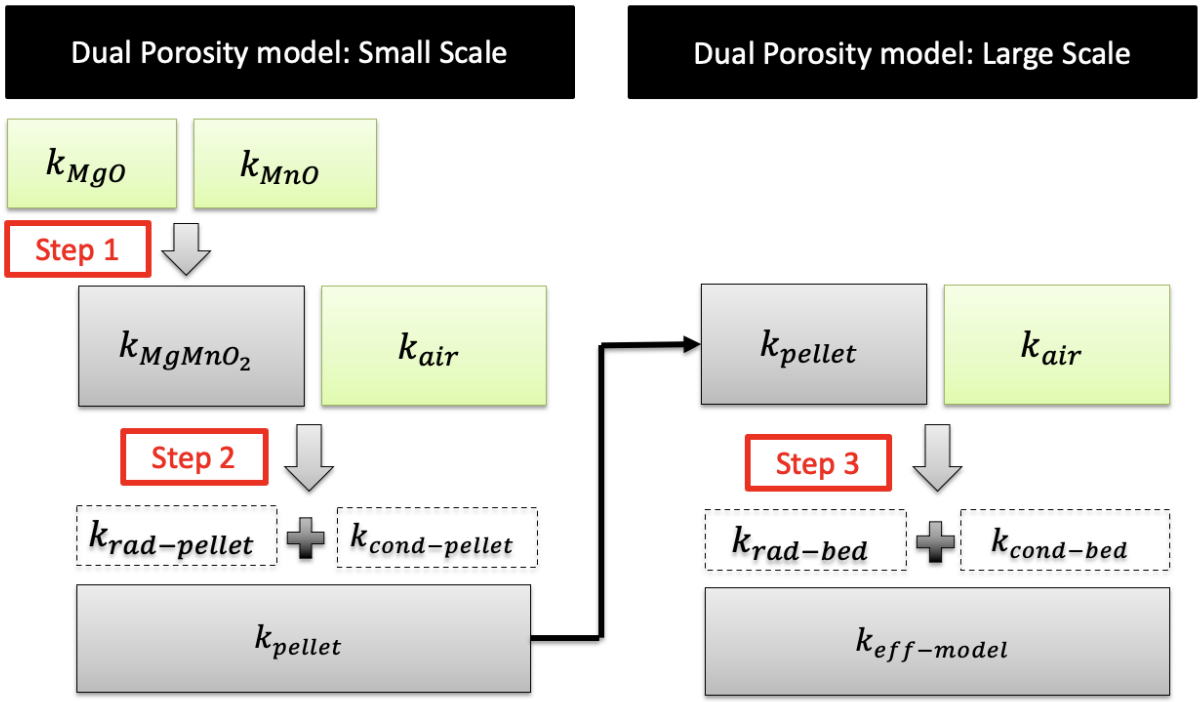

Figure 2.1: Theoretical modeling of the effective thermal conductivity of the packed bed of magnesium-manganese oxide pellets based on a dual-porosity method: Step 1 - Estimating the magnesium-manganese-oxide thermal conductivity based on its components, magnesium-oxide, and manganese-oxide, Step 2 - Estimating the effective thermal conductivity of a single pellet, step 3 - Estimating the effective thermal conductivity of the packed bed of magnesium-manganese-oxide pellet. Green blocks have known values from the literature, and the gray blocks are estimated through modeling.

2.1.1 Conduction Models

Conduction is the dominant mode of heat transfer in porous materials at low to moderate temperatures. The porous structure can significantly affect the heat transfer due to conduction. Numerous models have been suggested to predict the effective thermal conductivity due to conduction. These models come at different levels of complexity. In general, there is a trade-off between accuracy and

simplicity. In the following part, a few of these models will be introduced:

1- Parallel conduction model: The maximum value of the effective thermal conductivity of a two-phase system can be achieved when the solid and fluid phases are in parallel with the direction of heat flow. In this case, the effective thermal conductivity is:

$$k_{\text{cond}} = \phi k_f + (1-\phi)k_s \tag{2.2}$$

In which k_s is the thermal conductivity of solid, k_f is the thermal conductivity of the fluid, and ϕ is the porosity.

2- Series conduction model: The minimum value of effective thermal conductivty of a two-phase system can be achieved when the solid and fluid phases are normal to the direction of heat flow. In this case, the effective thermal conductivity can be found as follows:

$$k_{\text{cond}} = \frac{k_s k_f}{\phi k_s + (1-\phi)k_f} \tag{2.3}$$

3- Geometric mean model: This model considers the random distribution of the solid and fluid phases and estimates the effective thermal conductivity based on the weighted geometric mean of the conductivity of phases as follows:

$$k_{\text{cond}} = k_f^{\phi} k_s^{1-\phi} \tag{2.4}$$

4-Maxwell model: Maxwell used the potential theory to obtain the exact solution for thermal conductivity of randomly distributed and non-interacting homogeneous solid spheres as follows [20]:

$$k_{\text{cond}} = k_f \frac{2\phi k_f + (3-2\phi)k_s}{(3-\phi)k_f + \phi k_s} \tag{2.5}$$

This model is only applicable when the porosity is large.

5- Krupiczka model: Krupiczka derived a general model for granular materials based on the numerical solution of the effective thermal conductivity of a packed bed of long cylinders with porosity of 0.215 and spheres in a cubic lattice with porosity of 0.476. Taking into account the effect of porosity, he approximated these two solutions by the following general correlation:

$$k_{\text{cond}} = k_f \left(\frac{k_s}{k_f}\right)^{\left(0.28 - 0.757\log(\phi) - 0.057\log\left(\frac{k_s}{k_f}\right)\right)} \tag{2.6}$$

This correlation is valid for $0.215 < \phi < 0.476$.

6- Zehner and Schlunder model: This model is based on a one-dimensional heat flow through a packed bed of spherical particles. The effective thermal conductivity is estimated as follows:

$$k_{\text{cond}} = k_f \left(1 - (1-\phi)^{1/2} + \frac{2(1-\phi)^{1/2}}{1-KN} \left(\frac{(1-K)N}{(1-KN)^2} \ln\left(\frac{1}{KN}\right) - \frac{N+1}{2} - \frac{N-1}{1-KN} \right) \right) \tag{2.7}$$

in which

$$K = \frac{k_f}{k_s} \tag{2.8}$$

and

$$N = 1.25 \left(\frac{1-\phi}{\phi} \right)^{10/9} \tag{2.9}$$

7- Woodside and Messmer model: This model is suggested based on a combination of the series and parallel distribution as follows:

$$k_s = \frac{a_w k_s k_f}{k_s(1-d_w) + d k_f} + c_w k_f \tag{2.10}$$

in which,

$$c_w = \phi - 0.03, \tag{2.11}$$

$$a_w = 1 - c_w, \tag{2.12}$$

$$d_w = \frac{1-\phi}{a_w} \tag{2.13}$$

2.1.2 Radiation Model

The radiation component of the effective thermal conductivity can be calculated based on the Rosseland diffusion approximation [21, 22], as follows:

$$k_{\text{rad}} = \frac{16 n^2 \sigma T^3}{3\beta} \tag{2.14}$$

In which n is the refractive index of the medium, σ is the Stefan-Boltzmann constant, and β is the extinction coefficient. Extinction coefficients incorporates the specific radiation characteristics of

the porous material in the radiation model. Hsu and Howel [23] proposed the following model to predict the extinction coefficient of ceramic materials:

$$\beta = M \frac{(1-\phi)}{d_{\text{pore}}} \tag{2.15}$$

In which M is a constant coefficient.

They used a guarded hot-plate test apparatus to determine the effective thermal conductivity and radiative properties of partially stabilized zirconia (PS ZrO_2). The constant M was set to 3 by Hsu and Howell. Hendricks and Howell [21] determined absosrption and scattering coefficient as well as scattering phase function of PS ZrO_2 and oxide-bonded (OB) SiC porous materials, and noted that the extinxtion correlates betterm when M is set to 4.4 for PS ZrO_2, and 4.8 for OB SiC [24]. Zaversky et al. [25] used this correlation with $M = 4.8$ for their investigation of radiative heat transfer in SiC foams as solar absorbers.

It can be concluded that M is a material-specific parameter, and the exact value needs to be investigated for each material. Determination of the extinct coefficient of the packed bed of magnesium-manganese-oxide pellets is out of the scope of this thesis, so the radiation model is investigated for different extinction coefficients ($M = 4 - 10$) to find the best match with our experimental results.

2.2 Thermal conductivity of magnesium-manganese-oxide with zero porosity

Since there is no empirical data, the thermal conductivity of magnesium-manganese-oxide is estimated based on its components, magnesium-oxide, and manganese-oxide using a mixing rule. In this step, we will consider zero porosity for the mixture of magnesium-oxide and manganese-oxide, and we will refer to it as "$MgMnO_2$" throughout the thesis.

The thermal conductivity of manganese-oxide and magnesium-oxide is estimated as a function of temperature by curve-fitting to the experimental data, which is discussed in the following sections.

A_0	52.849
A_1	-0.1641
A_2	2.7056E-4
A_3	-2.4997E-7
A_4	1.2753E-10
A_5	-3.2666E-14
A_6	3.2900E-18

Table 2.1: Polynomial fitting coefficients to estimate magnesium-oxide thermal conductivity

2.2.1 Thermal conductivity of magnesium-oxide

In Figure 2.2, the empirical data for thermal conductivity of magnesium-oxide [1] are shown with black dots. A 6-th order polynomial is fitted through the experimental data (shown by the dashed line). The thermal conductivity of magnesium-oxide can be calculated as a function of temperature as follows:

$$k_{\mathrm{MgO}}(T) = \sum_{n=0}^{6} A_i T^i \tag{2.16}$$

The coefficient of this polynomial are given in Table 2.4.

2.2.2 Thermal conductivity of manganese-oxide

Similar to magnesium-oxide, the empirical data for manganese-oxide is obtained from Reference [1]. Since the empirical data is limited to temperatures below 800 °C, the thermal conductivity is extrapolated for temperatures higher than 800 °C. An exponential curve is fitted through the empirical data to estimate the thermal conductivity of manganese-oxide, as follows:

$$k_{\mathrm{MnO}}(T) = p \exp(q) \tag{2.17}$$

Coefficients of this exponential fit are given in Table 2.4.

2.2.3 Thermal conductivity of magnesium-manganese-oxide

After calculating the thermal conductivity of magnesium-oxide and manganese-oxide in 100 °C intervals, the thermal conductivity of $MgMnO_2$ is estimated using the geometric mean model,

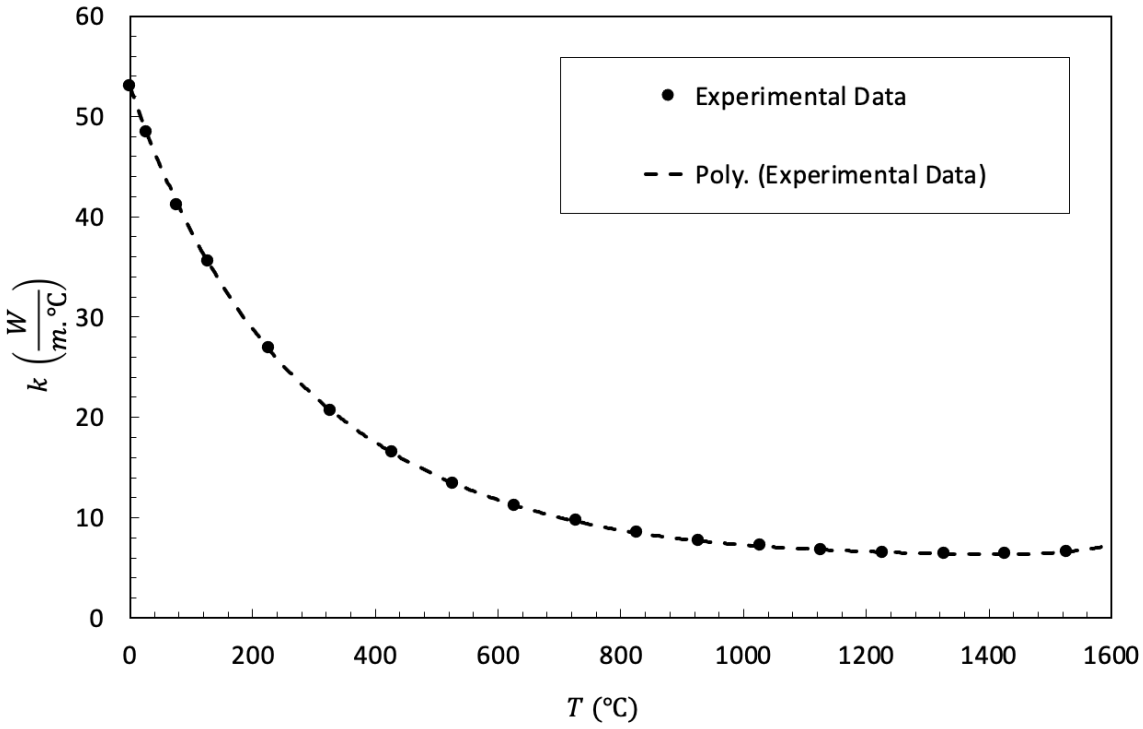

Figure 2.2: Thermal conductivity of magnesium-oxide: A 6th order polynomial is fitted through the empirical data [1], giving the magnesium oxide thermal conductivity as a function of temperature.

p	4.1893
q	-6.734E-4

Table 2.2: Exponential fitting coefficients to estimate manganese-oxide thermal conductivity

assuming the random distribution of magnesium-oxide and manganese-oxide powders in the solid mixing process. The geometric model is used as follows:

$$k_{\mathrm{MgMnO_2}} = k_{\mathrm{MgO}}^{\Phi} k_{\mathrm{MnO}}^{(1-\Phi)} \tag{2.18}$$

In which Φ is the volume fraction of magnesium-oxide in the magnesium-manganese-oxide mixture, equal to 0.460117. The calculated magnesium-manganese-oxide thermal conductivity versus temperature is shown in Figure 2.4.

In this step, the porosity is assumed to be zero, and is replaced by the volume fraction of com-

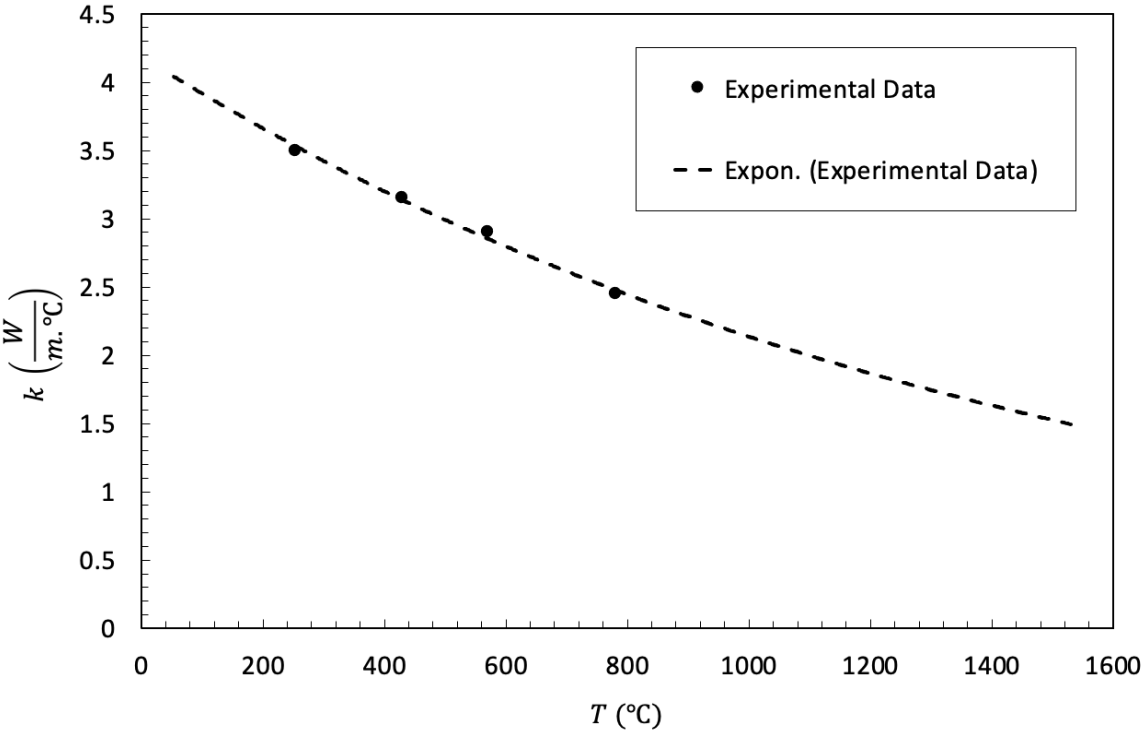

Figure 2.3: Thermal conductivity of manganese-oxide: An exponential curve is fitted through the empirical data, giving the manganese-oxide thermal conductivity as a function of temperature. No empirical data is found for temperatures over 800 °C, so the thermal conductivity in this region is estimated by extrapolation. [1]

ponents. Since there is no void space in the mixed material, the only contributing mode of heat transfer is conduction.

2.3 Effective thermal conductivity of a single pellet

After estimating the thermal conductivity of $MgMnO_2$, the effective thermal conductivity of a single porous pellet can be found as follows:

$$k_{\text{pellet}} = k_{\text{cond-pellet}} + k_{\text{rad-pellet}} \tag{2.19}$$

Considering the random structure of the porous, the geometrical mean model is used for the conduction mode in the pellet as well.

$$k_{\text{cond}} = k_{\text{air}}^{\phi_{\text{pellet}}} k_{\text{MgMnO}_2}^{(1-\phi_{\text{pellet}})} \tag{2.20}$$

T(°C)	k_{MgO}	k_{MnO}	k_{MgMnO2}
0	52.6885	4.1893	13.4260
50	45.1292	4.0506	12.2776
100	38.7461	3.9165	11.2395
150	33.3789	3.7868	10.3054
200	28.8841	3.6614	9.4683
250	25.1337	3.5402	8.7215
300	22.0144	3.4230	8.0579
350	19.4262	3.3096	7.4703
400	17.2818	3.2001	6.9515
450	15.5051	2.8926	5.7340
500	14.0308	2.9917	6.0905
550	12.8029	2.8926	5.7340
600	11.7743	2.7968	5.4179
650	10.9058	2.7042	5.1360
700	10.1653	2.6147	4.8830
750	9.5271	2.5281	4.6541
800	8.9709	2.4444	4.4455
850	8.4815	2.3635	4.2542
900	8.0479	2.2852	4.0779
950	7.6629	2.2096	3.9152
1000	7.3223	2.1364	3.7650
1050	7.0242	2.0657	3.6272
1100	6.7692	1.9973	3.5018
1150	6.5591	1.9312	3.3891
1200	6.3970	1.8672	3.2900
1250	6.2867	1.8054	3.2050
1300	6.2324	1.7456	3.1347
1350	6.2384	1.6878	3.0796
1400	6.3089	1.6319	3.0398
1450	6.4474	1.5779	3.0150
1500	6.6570	1.5257	3.0045

Table 2.3: Estimated values of $MgMnO_2$'s thermal conductivity based on a mean geometrical model, and its components, magnesium-oxide and manganese-oxide

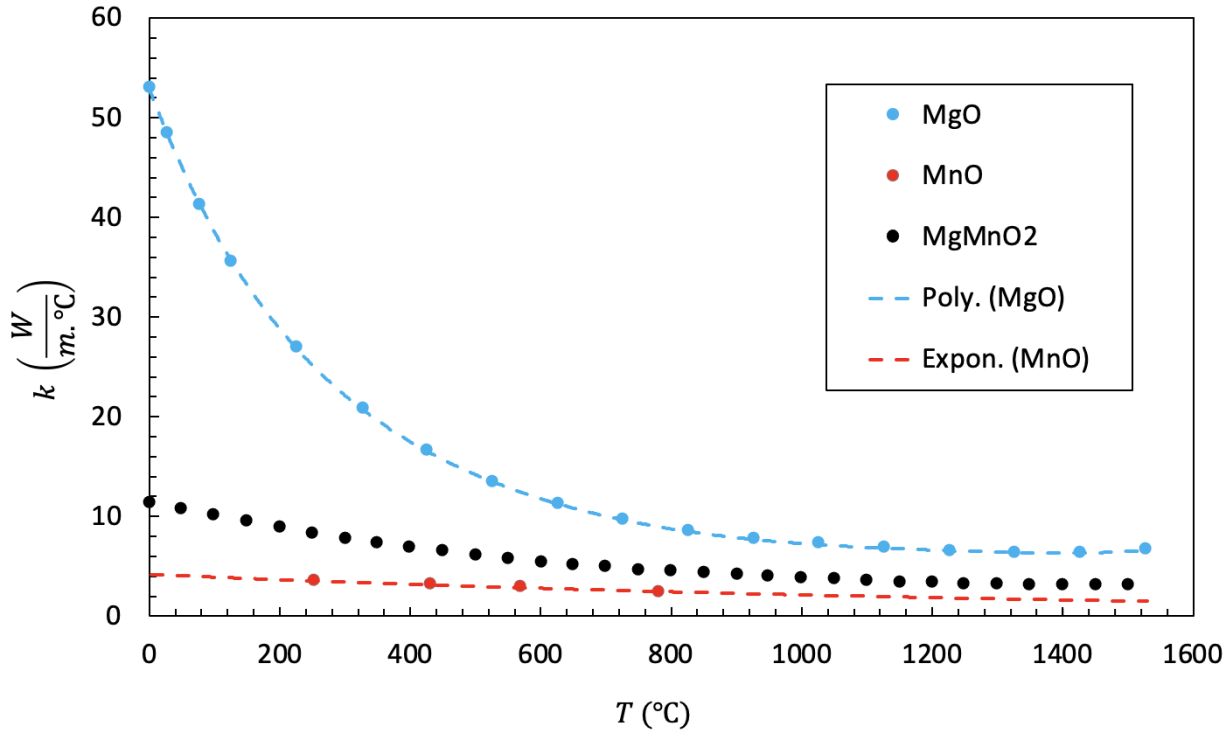

Figure 2.4: Estimated thermal conductivity of magnesium-manganese oxide based on a geometrical mean model versus temperature

In this equation, the thermal conductivity of $MgMnO_2$ is calculated from the previous step, the porosity of the pellet (ϕ_{pellet}) is equal to 0.264, and the thermal conductivity of air can be found by the following equation:

$$k_{\text{air}} = \sum_{n=0}^{2} B_i T^i \tag{2.21}$$

The radiation component is modeled using Rosseland diffusion approximation, as follows:

$$k_{\text{rad}} = \frac{16n^2\sigma T^3}{3\beta_{\text{pellet}}} \tag{2.22}$$

In which:

$$\beta_{\text{pellet}} = M_{\text{pellet}} \frac{1-\phi_{\text{pellet}}}{d_{\text{pore-pellet}}} \tag{2.23}$$

The radiation component is calculated with $M_{\text{pellet}} = 4$ to maximize the effect of radiation. As shown in Figure 4.5, even with the lowest coefficient, which will result in higher radiation effects, the

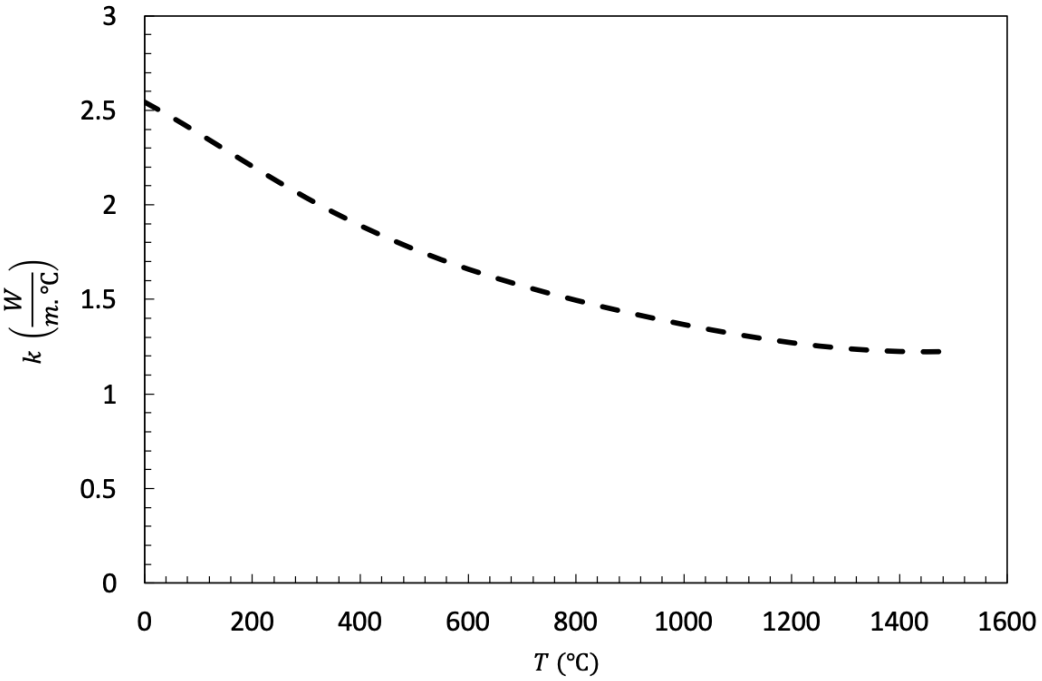

Figure 2.5: Effective thermal conductivity of a single pellet versus temperature: As shown, the radiation component does not affect the effective thermal conductivity of the pellet.

B_0	2.4674E-2
B_1	6.8601E-5
B_2	1.2242E-8

Table 2.4: Polynomial fitting coefficients to estimate air thermal conductivity

radiation component has no role in the pellet's effective thermal conductivity due to the microscale size of porous ($< 0.14\%$).

2.4 Effective thermal conductivity of the packed bed of magnesium-manganese-oxide pellets

After finding the pellet's effective thermal conductivity, the same procedure is followed to estimate the effective thermal conductivity of the packed bed of magnesium-manganese-oxide pellets. In this case, the solid phase is the pellet, and the porosity of the bed is 0.369. The effective thermal conductivity of the packed bed is estimated considering conduction and radiation

T(°C)	k_{MgMnO_2}	k_{air}	$k_{cond-pellet}$	$k_{rad-pellet}$	$k_{eff-pellet}$
0	13.4260	0.0247	2.5452	0.0000	2.5452
50	12.2775	0.0281	2.4657	0.0000	2.4657
100	11.2395	0.0314	2.3800	0.0000	2.3801
150	10.3054	0.0347	2.2921	0.0000	2.2921
200	9.4683	0.0379	2.2045	0.0000	2.2045
250	8.7215	0.0411	2.1194	0.0000	2.1195
300	8.0579	0.0442	2.0382	0.0001	2.0382
350	7.4703	0.0472	1.9618	0.0001	1.9619
400	6.9515	0.0502	1.8908	0.0001	1.8909
450	6.4939	0.0531	1.8254	0.0001	1.8255
500	6.0905	0.0559	1.7654	0.0001	1.7656
550	5.7340	0.0587	1.7106	0.0002	1.7108
600	5.4179	0.0614	1.6605	0.0002	1.6607
650	5.1360	0.0641	1.6144	0.0002	1.6147
700	4.8830	0.0667	1.5719	0.0003	1.5722
750	4.6541	0.0692	1.5324	0.0003	1.5328
800	4.4455	0.0717	1.4954	0.0004	1.4958
850	4.2542	0.0741	1.4605	0.0004	1.4609
900	4.0779	0.0765	1.4275	0.0005	1.4280
950	3.9152	0.0788	1.3962	0.0006	1.3967
1000	3.7650	0.0810	1.3666	0.0006	1.3673
1050	3.6272	0.0832	1.3390	0.0007	1.3397
1100	3.5018	0.0853	1.3134	0.0008	1.3142
1150	3.3891	0.0874	1.2902	0.0009	1.2911
1200	3.2900	0.0894	1.2699	0.0010	1.2709
1250	3.2050	0.0913	1.2527	0.0011	1.2538
1300	3.1347	0.0932	1.2390	0.0012	1.2402
1350	3.0796	0.0950	1.2292	0.0013	1.2305
1400	3.0398	0.0967	1.2233	0.0014	1.2248
1450	3.0150	0.0984	1.2216	0.0016	1.2231
1500	3.0045	0.1000	1.2237	0.0017	1.2254

Table 2.5: Estimated values of a single pellet effective thermal conductivity and its components, conduction, and radiation. The radiation component is calculated for $M_{pellet} = 4$

components, as follows:

$$k_{\text{bed}} = k_{\text{cond-bed}} + k_{\text{rad-bed}} \tag{2.24}$$

The radiation component is calculated as follows:

$$k_{\text{rad-bed}} = \frac{16n^2\sigma T^3}{3\beta_{\text{bed}}} \tag{2.25}$$

In which:

$$\beta_{\text{bed}} = M_{\text{bed}} \frac{1-\phi_{\text{bed}}}{d_{\text{pellet}}} \tag{2.26}$$

The radiation component of the packed bed effective thermal conductivity is calculated for different extinction coefficients ($M_{\text{bed}} = 4 - 10$), and the results are shown in Table 2.6. As shown, the radiation component is strongly dependent on the extinction coefficient in higher temperatures. Unlike the pellet, the radiation component of the packed is growing rapidly and becomes prominent in higher temperatures.

The conduction component is calculated for different models and the results are shown in Figure 2.6. In order to find the appropriate model for the conduction, the theoretical modeling results are compared with our experimental results, which will be discussed in the following chapters. The comparison is made at $T = 310°\text{C}$, the lowest temperature that the measurements are done. The lowest temperature is chosen to minimize the contribution of the radiation component to the packed bed effective thermal conductivity. Since the radiation component has a minor role, the conduction component is the dominant term in the packed bed effective thermal conductivity. The results of different modelings and experimental measurements are shown in Table 2.7.

The assumptions of parallel and series models are not realistic for the packed bed structure, and the predicted thermal conductivity is not close to the experimental results. However, these values are calculated to have an upper and lower limit for the packed bed. The geometric model assumptions are applicable to the packed bed. However, this model overpredicts the packed bed's effective thermal conductivity. The Krupiczka model is based on long cylindrical particles, which is close to the packed bed structure. The porosity of the packed bed is within the suggested range of porosity by the model, and it predicts the most comparative values to our experimental results. Due to

T(°C)	$k_{\text{rad-bed}}$ ($M_{\text{bed}} = 4$)	$k_{\text{rad-bed}}$ ($M_{\text{bed}} = 6$)	$k_{\text{rad-bed}}$ ($M_{\text{bed}} = 8$)
0	0.0092	0.0062	0.0046
50	0.0153	0.0102	0.0077
100	0.0236	0.0158	0.0118
150	0.0345	0.0230	0.0172
200	0.0482	0.0321	0.0241
250	0.0651	0.0434	0.0326
300	0.0857	0.0571	0.0428
350	0.1101	0.0734	0.0550
400	0.1388	0.0925	0.0694
450	0.1721	0.1147	0.0860
500	0.2103	0.1402	0.1051
550	0.2538	0.1692	0.1269
600	0.3029	0.2019	0.1515
650	0.3580	0.2387	0.1790
700	0.4194	0.2796	0.2097
750	0.4874	0.3250	0.2437
800	0.5624	0.3750	0.2812
850	0.6448	0.4299	0.3223
900	0.7348	0.4899	0.3674
950	0.8328	0.5552	0.4164
1000	0.9392	0.6261	0.4696
1050	1.0543	0.7029	0.5271
1100	1.1784	0.7856	0.5892
1150	1.3119	0.8746	0.6559
1200	1.4551	0.9701	0.7275
1250	1.6083	1.0722	0.8042
1300	1.7720	1.1813	0.8860
1350	1.9464	1.2976	0.9732
1400	2.1319	1.4212	1.0659
1450	2.3288	1.5523	1.1644
1500	2.5375	1.6917	1.2687

Table 2.6: Radiation component of the packed bed effective thermal conductivity for different extinction coefficients

T(°C)	Parallel	Series	Geometric	Krupiczka	Exp 1	Exp 2	Exp 3
310	5.4835	0.0873	1.3284	0.3150	0.4644	0.4722	0.4879

Table 2.7: The comparison between different conduction models and experimental results of the packed bed effective thermal conductivity

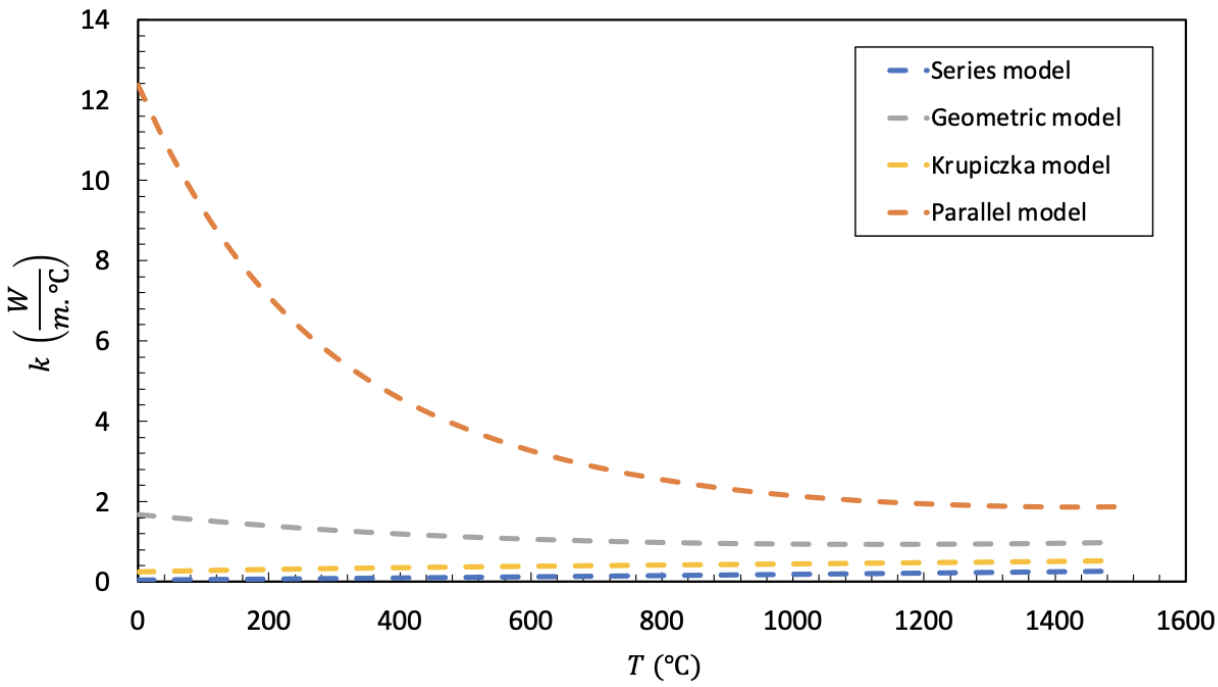

Figure 2.6: The conduction component of the packed bed's effective thermal conductivity calculated based on different models

these reasons, this model is chosen for the conduction component, even though it under-predicts the packed bed's effective thermal conductivity. This can be due to neglecting the radiation components or the assumption that we made to model the thermal conductivity of $MgMnO_2$.

This model is given as follows:

$$k_{\text{cond-bed}} = k_{\text{air}} \left(\frac{k_{\text{pellet}}}{k_{\text{air}}}\right)^{\left(0.28-0.757\log(\phi_{\text{pellet}})-0.057\log\left(\frac{k_{\text{pellet}}}{k_{\text{air}}}\right)\right)} \tag{2.27}$$

The effective thermal conductivity of the packed is calculated for different radiation components ($M_{\text{bed}} = 4 - 10$), and the results are shown in Figure 2.7. The rate of increase in the effective thermal conductivity of the packed in our experimental results (Table 5.3, 5.4, and 5.5) best matches the theoretical modeling when $M_{\text{bed}} = 6$. The radiation component is calculated for M_{bed}, is shown in Table 2.8, along with the conduction component and the overall effective thermal conductivity of the packed bed. These results are plotted in Figure 2.8, as it shows the conduction component is the dominant mode for temperatures below 900 °C. This component stays relatively constant in

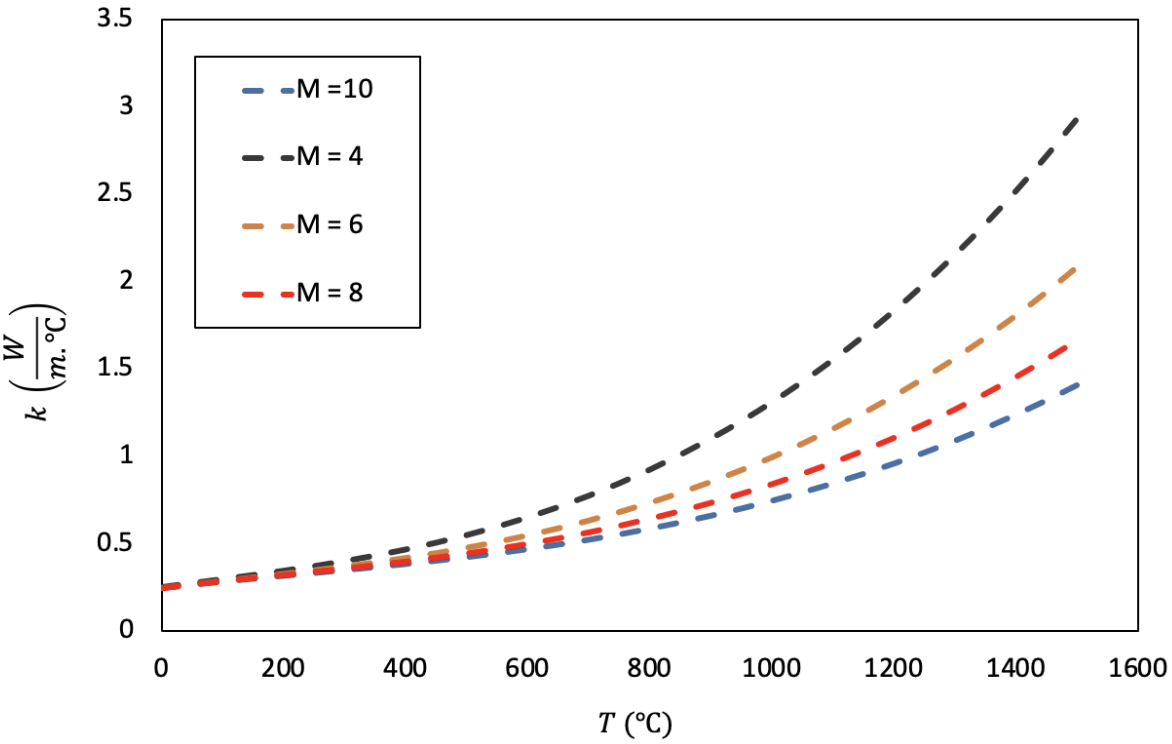

Figure 2.7: Effective thermal conductivity of the packed bed of magnesium-manganese-oxide pellets versus temperature for different extinction coefficients (M_{bed} = 6).

higher temperatures while the radiation component overgrows, so we can conclude that the rate of increase in the packed bed's effective thermal conductivity is attributed to the radiation component.

T(°C)	k_{pellet}	k_{air}	$k_{\text{cond-bed}}$	$k_{\text{rad-bed}}$	$k_{\text{eff-bed}}$
0	2.5452	0.0247	0.2426	0.0046	0.2472
50	2.4657	0.0281	0.2596	0.0077	0.2672
100	2.3801	0.0314	0.2742	0.0118	0.2860
150	2.2921	0.0347	0.2868	0.0172	0.3040
200	2.2045	0.0379	0.2976	0.0241	0.3217
250	2.1195	0.0411	0.3070	0.0326	0.3396
300	2.0383	0.0442	0.3152	0.0428	0.3580
350	1.9619	0.0472	0.3223	0.0550	0.3774
400	1.8909	0.0502	0.3287	0.0694	0.3980
450	1.8255	0.0531	0.3343	0.0860	0.4203
500	1.7656	0.0559	0.3393	0.1051	0.4445
550	1.7108	0.0587	0.3439	0.1269	0.4708
600	1.6607	0.0614	0.3481	0.1515	0.4996
650	1.6147	0.0641	0.3520	0.1790	0.5310
700	1.5722	0.0667	0.3555	0.2097	0.5652
750	1.5328	0.0692	0.3587	0.2437	0.6024
800	1.4958	0.0717	0.3616	0.2812	0.6428
850	1.4609	0.0741	0.3642	0.3224	0.6866
900	1.4280	0.0765	0.3665	0.3674	0.7339
950	1.3967	0.0788	0.3686	0.4164	0.7850
1000	1.3673	0.0810	0.3704	0.4696	0.8400
1050	1.3397	0.0832	0.3721	0.5271	0.8992
1100	1.3142	0.0853	0.3736	0.5892	0.9628
1150	1.2911	0.0873	0.3752	0.6559	1.0311
1200	1.2709	0.0894	0.3768	0.7275	1.1043
1250	1.2538	0.0913	0.3786	0.8042	1.1828
1300	1.2402	0.0932	0.3182	0.8860	1.2042
1350	1.2305	0.0950	0.3830	0.9732	1.3562
1400	1.2248	0.0967	0.3858	1.0659	1.4517
1450	1.2231	0.0984	0.3890	1.1644	1.5534
1500	1.2254	0.1000	0.3304	1.2687	1.5991

Table 2.8: Effective thermal conductivity of the packed bed of magnesium-manganese-oxide pellets and its components, conduction, and radiation.

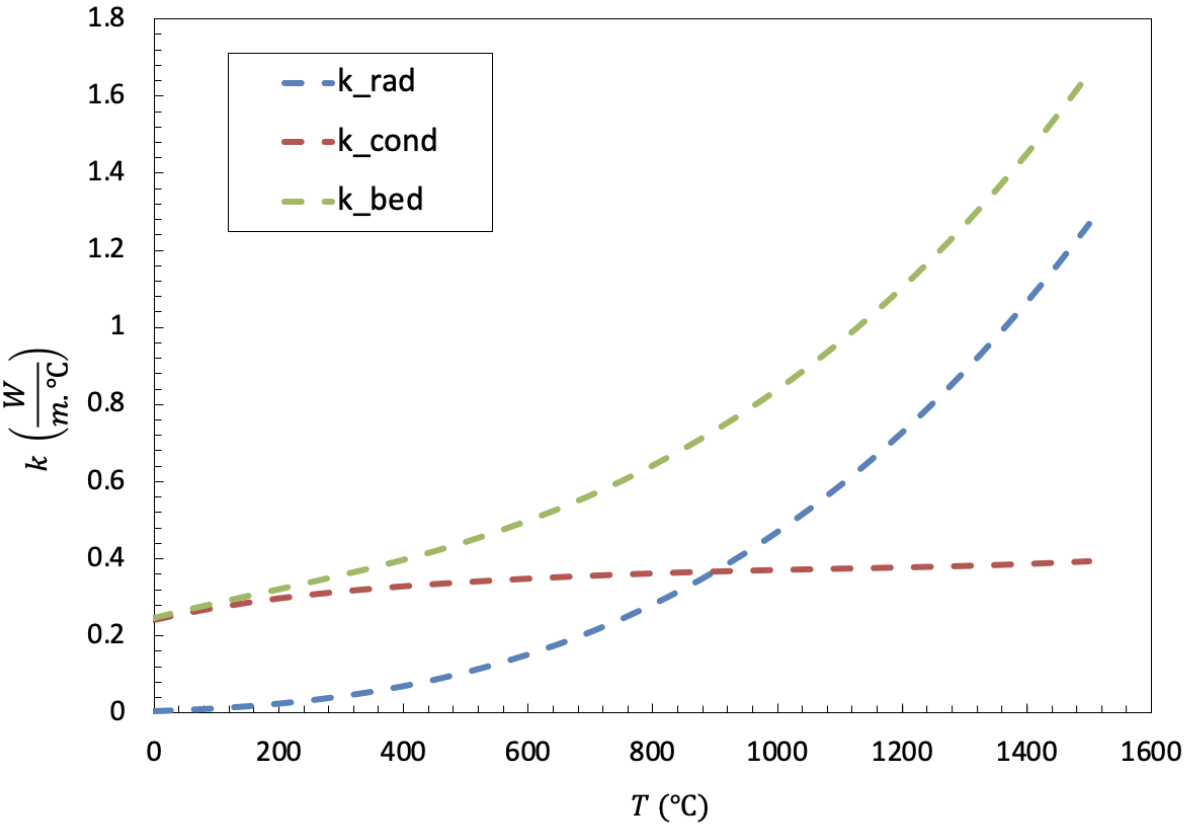

Figure 2.8: Effective thermal conductivity of the packed bed of magnesium-manganese-oxide pellet versus temperature, and its components, conduction, and radiation (for $M_{\text{bed}} = 6$). As shown in the figure, the radiation component grows rapidly with temperature and is the dominant mode in higher temperatures.

CHAPTER 3

TRANSIENT HOT-PROBE METHOD

3.1 Introduction

The transient hot-wire method is one of the most common and well-established methods for measuring thermal conductivity [26]. This method uses the rate of temperature change of a 1-D heat source embedded in the material to determine the effective thermal conductivity. This method has been used widely due to its simplicity and adopted for measuring the effective thermal conductivity of different materials [8].

Van der Held et al. [27, 28] developed an apparatus to determine the thermal conductivity of liquids using transient methods. Blackwell [29] recognized inadequacies in the mathematical analysis of the transient hot-wire method in some applications, as follows:

1- The assumption of line-source of heat, which is not generally valid, e.g., in geophysical applications.

2- Neglecting thermal contact resistance between the hot probe and the external medium.

3- Semi-empirical estimation of the minimum probe length to ensure radial flow conditions.

He revised the theory and the experimental method accordingly and proposed a modified transient method to determine the thermal conductivity of insulating materials. He also derived a condition for the minimum probe length to radius ratio to avoid significant errors due to axial heat losses [30].

Vos [2] discussed a few aspects of the transient hot-wire method, for example, the necessary conditions to hold the linear relationship between the temperature rise of hot wire and $\ln(t)$. He also defined an upper and a lower limit for the linear section. The temperature rise and $\ln(t)$ can deviate from a linear due to different reasons. One of the reasons of deviation is the inhomogeneity of the material. In this case, long-duration measurements are necessary to reflect the material's average thermal conductivity.

Jaeger [31] improved the hot-probe technique by measuring the temperature rise at a defined dis-

tance from the linear heat source. Vries [32] extended this theory to the case of a homogeneous probe of finite conductivity with a line source embedded in its center.

3.2 Theory

The three-dimensional, homogeneous differential equation of heat conduction in the cylindrical coordinate system assuming constant properties is given by:

$$\frac{\partial^2 T}{\partial r^2} + \frac{1}{r}\frac{\partial T}{\partial r} + \frac{1}{r^2}\frac{\partial^2 T}{\partial \phi^2} + \frac{\partial^2 T}{\partial z^2} = \frac{1}{\alpha}\frac{\partial T}{\partial t} \tag{3.1}$$

If the temperature is independent of z and ϕ direction, the differential equation can be simplified to the transient 1-D heat conduction differential equation as follows:

$$\frac{\partial^2 T}{\partial r^2} + \frac{1}{r}\frac{\partial T}{\partial r} = \frac{1}{\alpha}\frac{\partial T}{\partial t} \tag{3.2}$$

This equation can be solved for different boundary and initial conditions.

The external medium can be modeled as a 1-D infinite hollow cylinder with an inner diameter of $2R_s$, in which R_s is the outer diameter of the hot probe. The temperature of the external medium can be found by solving the transient, 1-D heat conduction equation considering the following boundary conditions.

1- Constant heat flux at $r = R_s$ (due to the constant heat generation in the hot probe).

2- Infinite hollow cylinder (The external medium's radius is much larger than the hot probe).

The general solution for the temperature distribution is given by [16]:

$$T(r,t) = \frac{Q}{4\pi k}\int_{t_0}^{t} \frac{1}{t-t_0} \exp\left(\frac{r^2 + R_s^2}{4\alpha(t-t_0)}\right) I_0\left(\frac{rR_s}{2\alpha(t-t_0)}\right) dt \tag{3.3}$$

In which α is the thermal diffusivity, and I_0 is the modified Bessel function of zero order.

Knowing the heat flux and the transient temperature at any point of the medium, the thermal conductivity can be calculated by solving Equation 3.3. However, this equation has a complex form, and further simplification can be done.

Marmoret et al.[16] used the following general solution to the transient, 1-D heat conduction

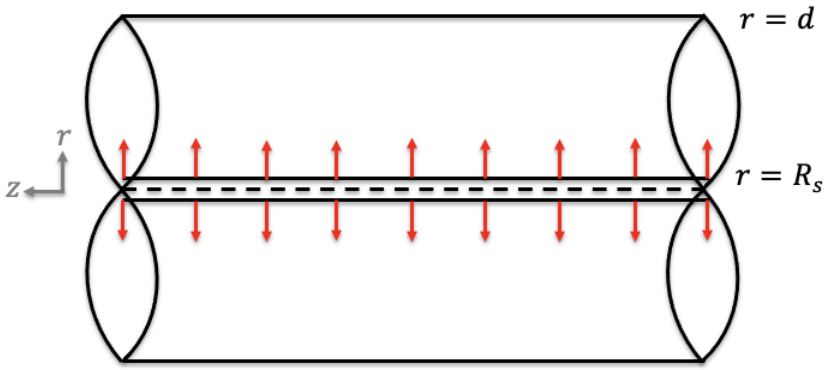

Figure 3.1: A schematic of the external medium: the external medium is modeled as an infinite hollow cylinder with constant heat flux at the inner boundary

equation to estimate the thermal conductivity as follows:

$$\frac{kT}{Q} = G(Fo, \Omega, Bi) = \frac{8\Omega^2}{\pi^3} \int_0^\infty \frac{1 - \exp(-Fo.x^2)}{x^3 \Delta(x)} \, dx \tag{3.4}$$

In which,

$$\Delta(x) = \left[xJ_0(x) - \left(2\Omega - \frac{x^2}{Bi} \right) J_1(x) \right]^2 + \left[xY_0(x) - \left(2\Omega - \frac{x^2}{Bi} \right) Y_1(x) \right]^2 \tag{3.5}$$

In this equation, J_0 and J_1 are the Bessel functions of the first kind of order 0 and 1, Y_0 and Y_1 are Bessel functions of the second kind of order 0 and 1.

This solution is expressed in the form of three non-dimensionalized numbers: Biot number (Bi), Fourier number (Fo), and Interia contrast (Ω). The contact resistance of the air conductance (R_c) is considered in the equation as well. These three dimensionless parameters are introduced in the following paragraphs:

Biot number (Bi): In general, the Biot number represents the ratio between thermal resistance by conduction and thermal resistance by convection at the body's surface. The Biot number smaller than 0.1 implies that the heat conduction inside the body is much faster than the heat convection outside, so the temperature gradient is negligible inside the body. In the hot probe application, the Biot number can be calculated based on thermal conductivity (k), probe volume (V_s), probe surface

(A_s), and probe length (I_s), as follows:

$$Bi = \frac{\frac{V_s/A_s}{kA_s}}{\frac{1}{HA_s}} = \frac{R_s}{k.R_c} \tag{3.6}$$

In which H is the conductance, the inverse of the contact resistance (R_c).

Fourier number (Fo): The Fourier number determines the ratio of the heat conducted through the medium and the heat stored in the material and is defined as follows:

$$Fo = \frac{\alpha.t}{R_s^2} \tag{3.7}$$

Inertia contrast (Ω): Inertia contrast represents the ratio between the heat capacity of the material (S_m) and the heat capacity of the probe (S_s), which is equal to:

$$\Omega = \frac{S_s}{S_m} = \frac{\pi R_s^2 \rho_s C_s}{S_m} \tag{3.8}$$

Knowing the temperature profile at the external surface of the hot probe, the three non-dimensionalized numbers, Bi, Fo, and Ω, can be estimated by taking the inverse of the integral using optimization methods. Subsequently, the contact resistance (R_c), thermal conductivity (k), and thermal diffusivity (α) can be calculated.

Marmoret et al. [16] demonstrated that this method accurately predicts the properties of glass wool. However, the complex form of the general solution is a drawback for this analysis method.

Blackman [29] derived the approximated solution of the hot probe temperature at small- and large-time. The large-time solution gives the temperature of the probe as a function of time, as follows:

$$\Delta T_m(t) \approx A \ln(t) + B + \frac{1}{t}\{C \ln(t) + D\} \tag{3.9}$$

In which ΔT_m is the temperature rise of the probe, t is time, and A, B, C, and D are constant coefficients, which can be derived from the following equations:

$$A = \frac{Q}{4\pi k} \tag{3.10}$$

$$B = \ln\left(\frac{4\alpha}{R_s^2}\right) - \gamma + \frac{2kR_c}{R_s} \tag{3.11}$$

$$C = \left(\frac{r^2}{2\alpha}\right)\left[1 - \left(\frac{m_{\text{probe}} c_p \alpha}{\pi R_s^2 k}\right)\right] \tag{3.12}$$

$$D = \left(\frac{r^2}{2\alpha}\right)\left[\ln\left(\frac{4\alpha}{R_s^2}\right) - \gamma + 1 - \frac{\left[\ln\left(\frac{4\alpha}{r^2}\right) - \gamma + \frac{2k}{R_s H}\right] m_{\text{probe}} c_p \alpha}{\pi R_s^2 L k}\right] \tag{3.13}$$

In which Q is the probe power per length, k is the effective thermal conductivity, α is the thermal diffusivity, R_s is the probe radius, γ is Euler's constant equal to 0.5772, m_{probe} is the mass of the probe, and C_p is the specific heat capacity of the probe.

In large-time, terms related to C and D become insignificant, so Equation 3.9 can be simplified as follows:

$$\Delta T_m = \frac{Q}{4\pi k} \ln(t) + B' \tag{3.14}$$

In which,

$$B' = \frac{Q}{4\pi k} B \tag{3.15}$$

So the thermal conductivity can be derived as follows:

$$k = \frac{Q}{4\pi \left(T(t_{\max}) - T(t_{\min})\right)} \ln\left(\frac{t_{\max}}{t_{\min}}\right) \tag{3.16}$$

As mentioned before, Blackman's analysis is based on the long-time assumption, so a lower limit on time needs to be considered for this analysis. This lower limit ($t_{\min}$) is associated with heating the 1-D hot probe evenly and heat flux propagation in the external medium. In materials with a non-homogeneous structure, the minimum time to reach the equilibrium state is higher than homogeneous materials, to neglect the spatial effect of the external medium.

An upper limit on time ($t_{\max}$) is needed as well. Since the radius of the external medium is finite

(even though it is much larger than the hot probe radius), the heat flux will eventually reach the outer boundary and starts leaking out. Since the hot probe method is developed based on the heat conduction of an infinite cylinder, this equation does not hold up when the heat reaches the boundary.

Vos [2] suggested the following lower and upper limits for the time:

$$t_{\min} = \frac{50R_s^2}{4\alpha}$$
$$t_{\max} = \frac{0.6d}{4\alpha}$$

However, the ASTM standard [33] suggests considering the most linear part of the $(\Delta T_m - \ln t)$ plot to calculate the thermal conductivity whenever the curve deviates from linearity.

CHAPTER 4

EXPERIMENTAL METHODS

4.1 Material

Figure 4.5 shows a picture of magnesium-manganese-oxide pelletst. The magnesium-manganese-oxide pellets are synthesized by a solid-state mixing method followed by heat treatment. First, the magnesium-oxide powder is mixed with manganese-oxide using a cement mixer. Cylindrical zirconia milling media is added to assist in the mixing process. Mixing takes about 3 to 4 hours. The mixed powder is pelletized using an automatic pellet press (TDP 5 Desktop Tablet Press from LFA machines).

When the mixing process is completed , the pressed pellets are heat treated in a box furnace. Heat treatment is performed at 1500 °C for 24 hours followed by 4 hours at 1000 °C. The physical properties of magnesium-manganese-oxides are listed in Table 4.1.

Figure 4.1: Magnesium-manganese-oxide pellets: These pellets are made by solid-state mixing of the magnesium- and manganese-oxide followed by a heat-treatment process. The mixed powder is added the mixed powder to an automatic pellet press.

Diameter (mm)	3.7
Height (mm)	3
porosity	0.264
Porous diameter (mm)	0.0003

Table 4.1: Magnesium-manganese-oxide pellet's physical properties

4.2 Experimental Setup

The experimental setup and hot probe are designed based on ASTM C1113 standard [34]. In a commercial heating probe, the temperature measurement device is packed with the 1-D heat source. But in this thesis, we used the platinum wire both as the heat generation source and the temperature measurement device as it is suggested ASTM C1113 [34]. In the following section, the design of the hot probe is explained.

4.2.1 Hot Probe

A 0.5 mm diameter platinum wire with 99.95% purity (SigmaAldrich), covered with a thin alumina sheet, is used both as the hot probe and the temperature measurement device. Heat is generated by passing a constant current through the platinum wire, and the platinum wire's temperature is calculated by measuring the wire's electrical resistance. The thin alumina sheet insulates the platinum's wire from to packed bed to prevent the electrical current leakage since magnesium-manganese-oxide pellets are electrically conductive at higher temperatures.

Platinum is chosen as the wire material because of its advantageous properties. First, the platinum's melting temperature is very high (1768 °C), making it a perfect candidate for high-temperature experiments; second, platinum is chemically stable and does not oxidize in higher temperatures; and third, The electrical resistance of platinum is known to have high accuracy and can be represented as a second-order polynomial of temperature. So, by knowing the wire's electrical resistance, the temperature can be calculated with high accuracy.

Two secondary platinum wires with the same purity are welded on both sides of the platinum wire's

center with a distance of 7.5 cm for voltage measurements. It is crucial to have the same material for the secondary wires as the primary wire to avoid measurement errors due to the Seebeck effect. The wire resistance can be calculated by measuring the voltage across the secondary wires and dividing by the current passed through the primary wire. Even though this small portion is used for the measurements, both primary and secondary wires are extended out of the furnace. The primary platinum wire (the heat generation source) is extended to prevent melting and oxidation, and the secondary wires are continued to avoid the Seebeck effect at elevated temperatures.

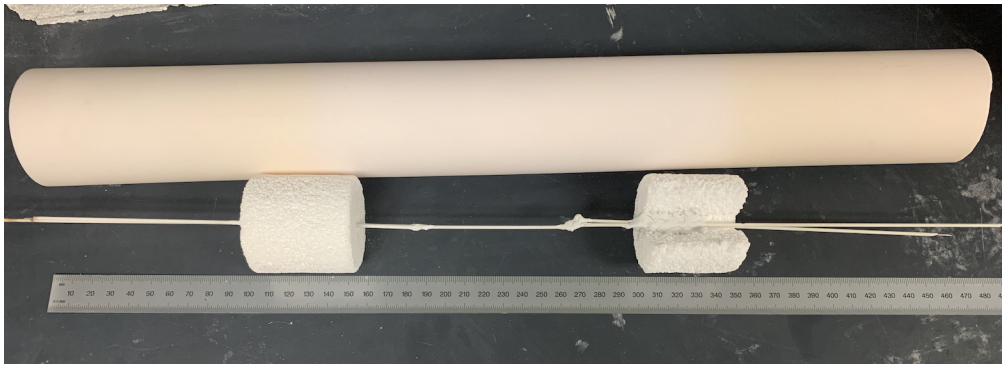

Figure 4.2: A picture of the hot probe: The primary platinum wire with a diameter of 0.5 mm is covered by a thin alumina sheet (OD = 1.7 mm), and used both as the 1-D heat generation source and the temperature measurement device. Two secondary platinum wires with the same purity are welded across the center for voltage measurement. As shown, both primary and secondary wires are extended out of the test container.

4.2.2 Test Apparatus

The experimental setup is designed based on ASTM C1113 standard [34]. Figure 4.3 shows a schematic of the test apparatus.

The bed space is made by placing two low thermal conductive bricks with a distance of 15 cm. A small hole is placed at the center of one of the bricks to insert the hot probe. On the other brick, a sector with an angle of 45° is removed to pack the pellets. After placing the hot probe at the center of the bricks, alumina paste is applied to secure the hot probe's location. After drying the paste, the hot probe and the insulation bricks are slid into the test container (An alumina tube

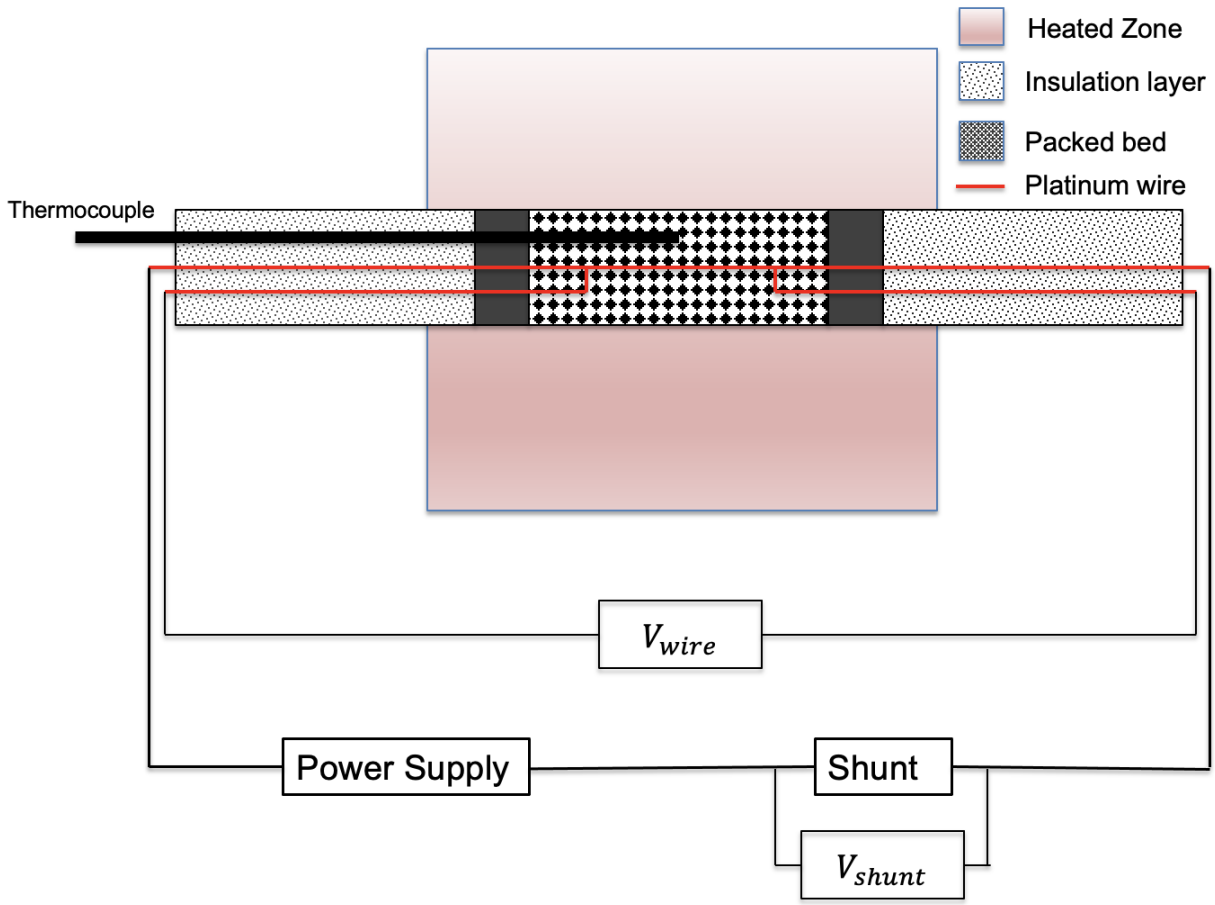

Figure 4.3: A schematic of test apparatus: A constant current generated by a DC power supply passed through the primary platinum wire. The voltage across the shunt and the secondary platinum wire is measured to calculate the current and the electrical resistance of the primary wire. A B-type thermocouple is inserted inside the packed bed to measure the bed temperature. Insulation materials are inserted outside of the insulation bricks to prevent heat loss from the ends.

with an inner diameter of 2 inches). The insulation material is packed outside of the insulation brick without the empty sector to secure the bricks' location. Then the packing of the pellets is achieved by pouring and shaking. A B-type thermocouple is inserted inside the packed bed during the packing process. After packing the bed, the insulation material is placed outside the second insulation brick to prevent heat loss from the container's end. Finally, the test container placed in a tube furnace (Sentrotech, Model: STT-1600 °C-12) [35], to perform the calibration and experiment process. The physical dimensions of the test setup are shown in Table 4.2.

After placing the test container in the tube furnace, the primary platinum wire is connected to

Bed length (cm)	15
Container ID (in)	2
container length (cm)	46
platinum wire length (cm)	7.5
platinum wire diameter (mm)	0.5
Probe OD (mm)	1.7
Bed porosity	0.369

Table 4.2: Test setup dimension

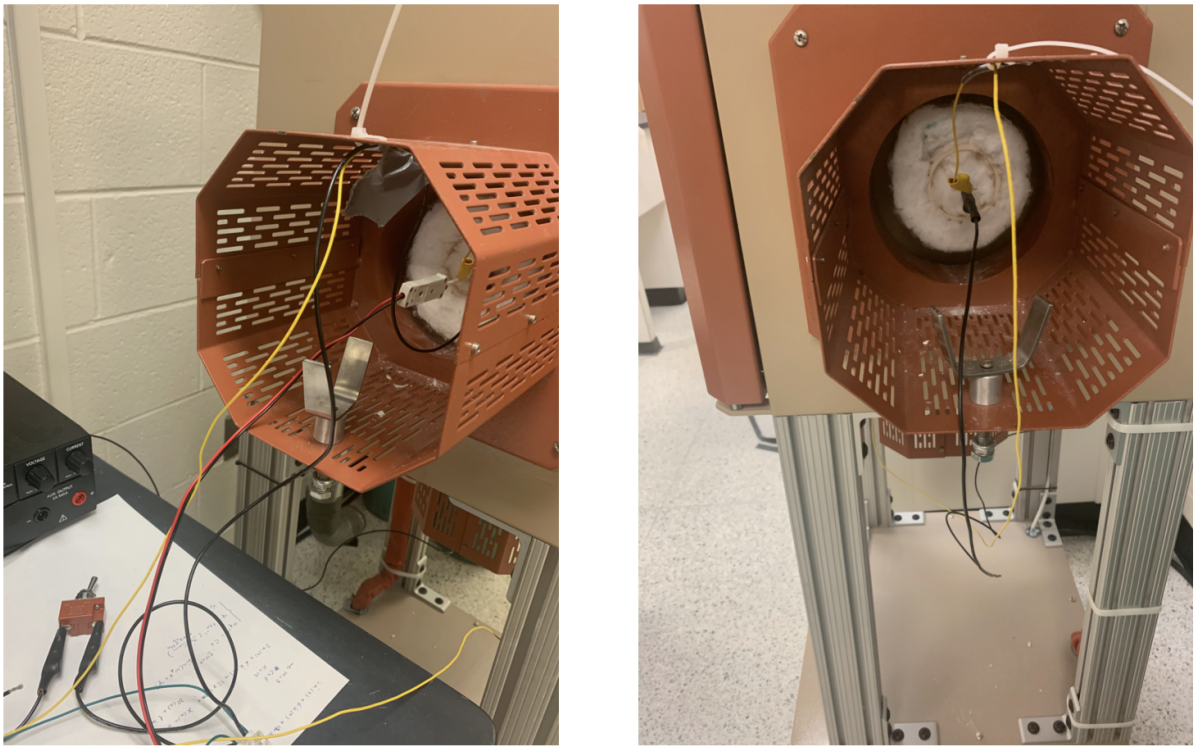

Figure 4.4: Test container in the tube furnace: The thermocouple and voltage measurement wires are connected to a LabJack T7 pro. Two compressed air tubes were installed outside the tube furnace to promote the cooling process.

a DC power supply, with a shunt placed in series downstream of the platinum wire. The voltage across the shunt and the platinum wire is measured by the data acquisition system. The current in the circuit is calculated by measuring the voltage across the shunt, as follows:

$$I = \frac{V_{\text{shunt}}}{R_{\text{shunt}}} \tag{4.1}$$

And respectively, the resistance of the platinum wire is calculated as follows:

$$R_{\text{wire}} = \frac{V_{\text{wire}}}{I} \tag{4.2}$$

Kipling [36] is used as the data acquisition software. The LabJack T7 pro's precision is limited by the recording frequency. For our experiment, the precision is far more important than frequency, so the precision is set to the highest degree, and subsequently, the recording frequency is set to 2 Hz. This frequency is fast enough for our application.

4.3 Calibration

Calibration is conducted per C1113 standard [34]. The purpose of calibration is to find the electrical resistance of the platinum wire as a function of temperature by fitting a second-order polynomial to the experimental electrical resistance measurements. Calibration measurements are performed in 100 °C intervals, starting from 300 °C and ending at 1300 °C. The following procedure is followed for each measurement:

The furnace is ramped up from the initial temperature with a rate of 10 °C per minute. Once the desired temperature is reached, the furnace is dwelled for 4 hours to stabilize temperature throughout the packed bed. After stabilizing the temperature, a $0.05A$ current is passed through the platinum wire. This current is low enough to ensure the wire's temperature is not rising significantly with respect to the packed bed. The voltage across the wire and the calibration shunt (100 Ω) is recorded for 30 s. The wire's electrical resistance is calculated and plotted versus the packed bed's temperature, measured by the B-type thermocouple. Once the wire resistance is calculated, the setup is ready to move to the subsequent measurement.

After conducting the calibration procedure for all temperatures, a second-order polynomial is fitted through the experimental measurements to obtain the calibration curve.

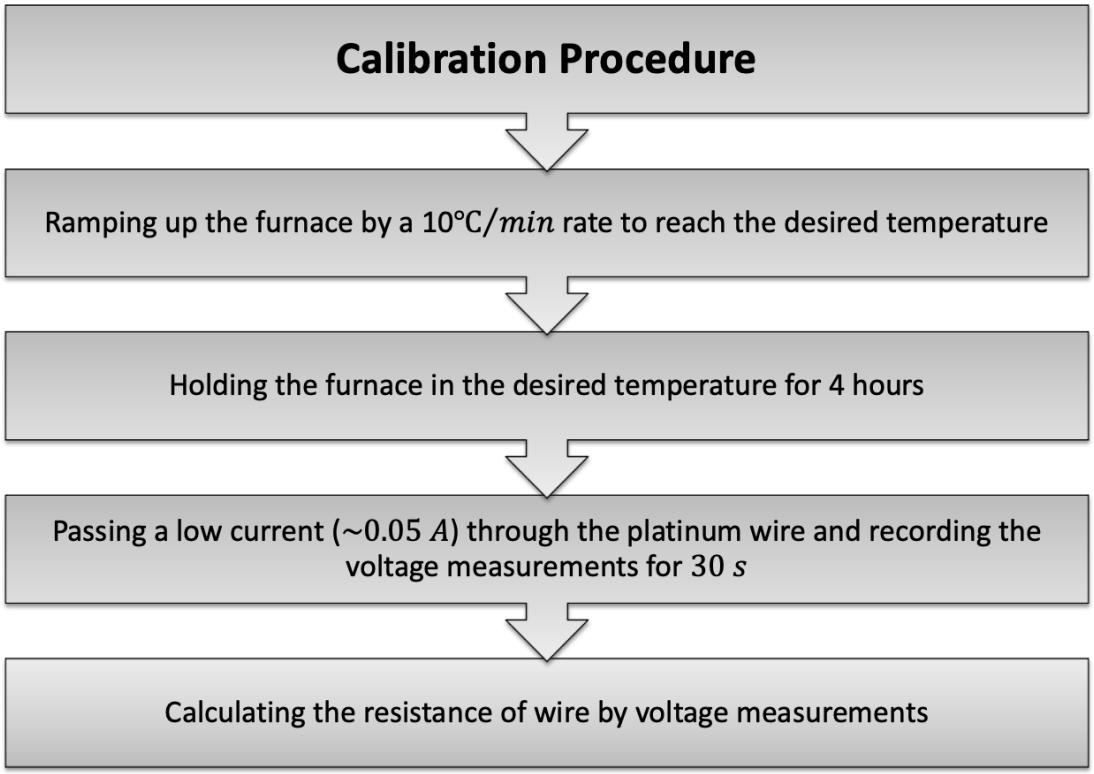

Figure 4.5: A schematic of the calibration procedure for each measurement.

4.4 Test Method

Similar to the calibration procedure, the furnace is ramped up from the initial temperature to reach the desired temperature with a rate of 10 °C per minute. Once the desired temperature is reached, the furnace is dwelled for 4 hours to stabilize the temperature of the test section. After keeping the furnace at a constant temperature for four hours, a constant current (3.8 to 4.2 A), is passed through the platinum wire for 300 seconds. Unlike the calibration, this current is high enough to raise the platinum wire's temperature with respect to the packed bed. During this period, the bed's temperature, the voltage across the shunt, and the voltage across the platinum wire are recorded, and the electrical resistance of the platinum wire is calculated based on the voltage measurements. This procedure is repeated from 300 to 1300 °C in 100 °C intervals for three experiments. An additional measurement at 1400 °C is done in experiment 3 as the final measurement.

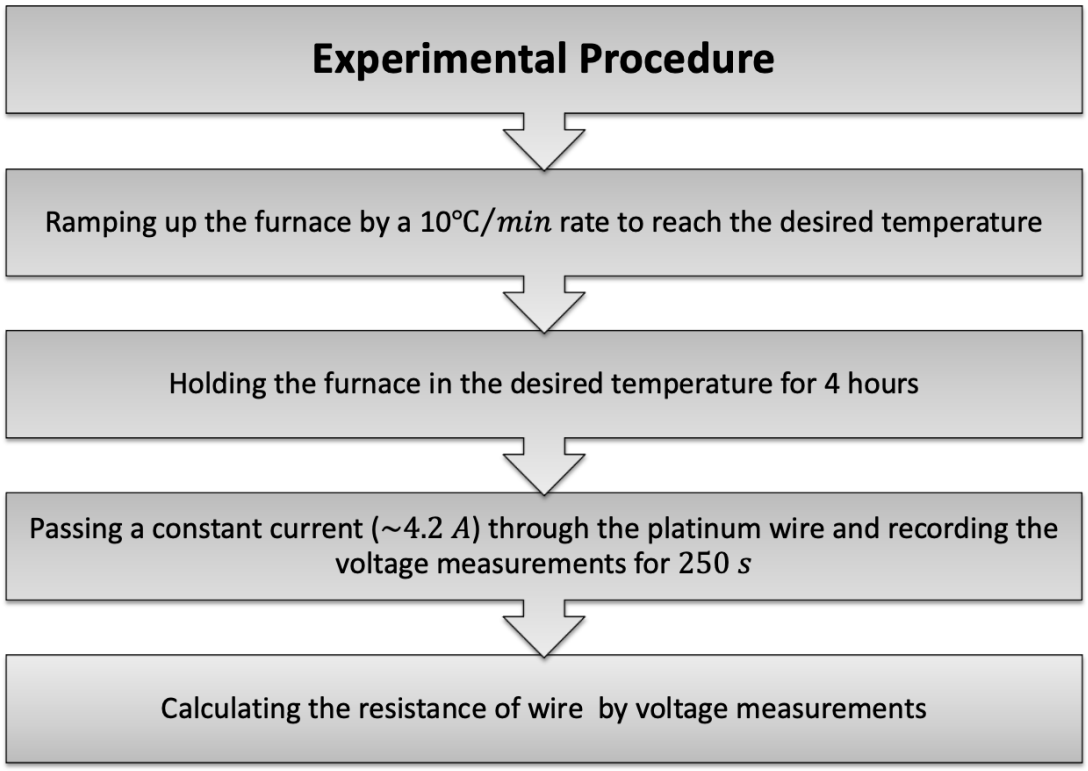

Figure 4.6: A schematic of the experimental procedure

CHAPTER 5

RESULTS AND DISCUSSION

5.1 Calibration

The platinum wire's electrical resistance at different temperatures is shown in Table 5.1. A second-order polynomial curve is fitted through the experimental data. The inverse of this curve predicts the platinum wire's temperature as a function of electrical resistance as follows:

$$T_m = a_1 + a_2\sqrt{a_3 + a_4 R} \tag{5.1}$$

The values of a_1 to a_4 are shown in Table 5.2.

The polynomial fitting has an R^2 of 0.999978, showing the high accuracy of the calibration process. The measured electrical resistance values are compared to the calculated resistance based on the resistivity data from the literature [37], showing excellent agreement (Figure 5.1). The calibration process was repeated three times at different stages of the experiment, resulting in similar calibration curves.

$T(°C)$	$R(\Omega)$
314.26	0.082391
411.69	0.095537
510.28	0.108342
608.07	0.120451
704.28	0.132164
801.65	0.143497
900.21	0.154493
1000.92	0.165161
1095.94	0.175056
1191.87	0.184905
1288.40	0.193665

Table 5.1: The electrical resistance of the platinum wire at various temperatures measured in the calibration process

a_1	3353.6170
a_2	-8.8508E-12
a_3	1.6495E+29
a_4	-5.7281E+29

Table 5.2: Calibration curve coefficients

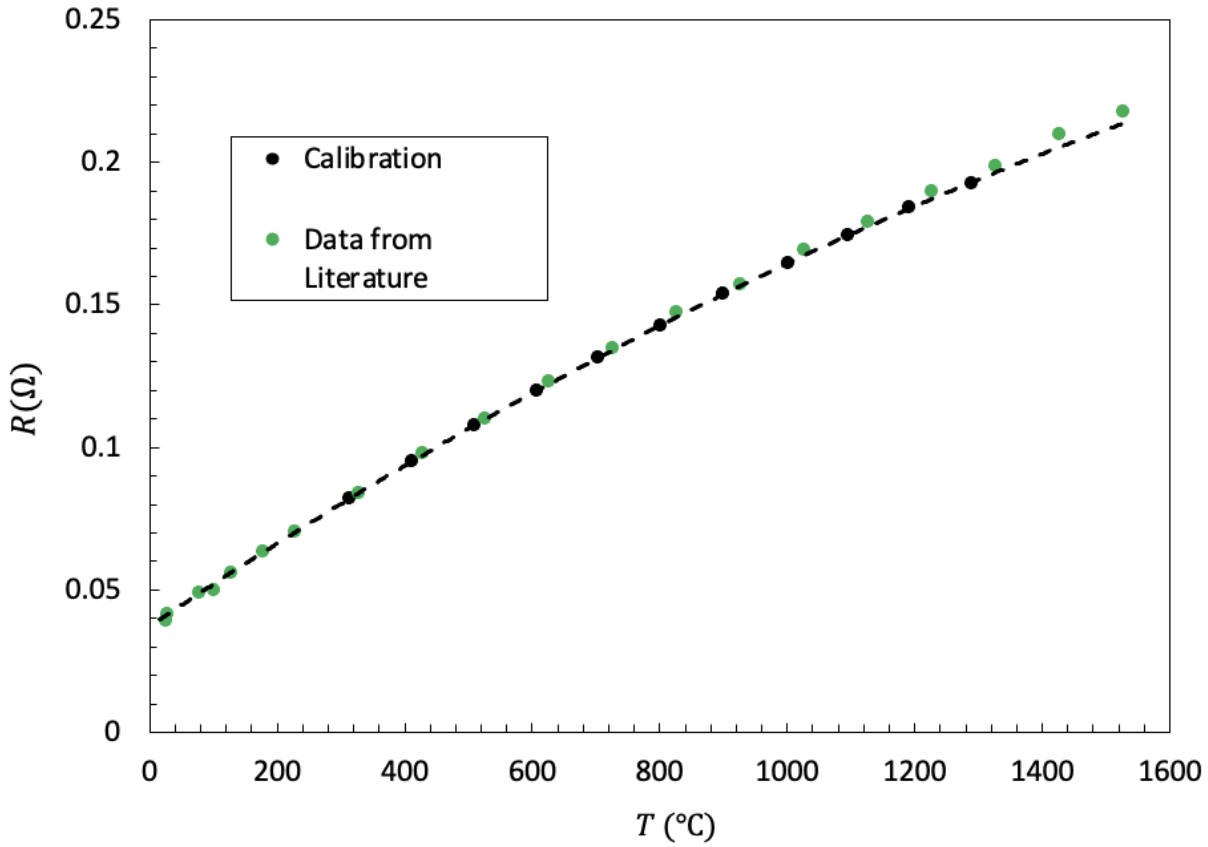

Figure 5.1: Calibration Process: The experimental data are shown with black dots. A second-order polynomial curve is fitted through the experimental data, displayed by the dashed line. The experimental resistance data are compared to the calculated values based on the electrical resistivity of platinum from the literature (shown in green dots), offering excellent agreement.

5.2 Experimental results

Once the data for each measurement is collected, the following steps are taken for data analysis. First, the wire's temperature is calculated based on the wire's electrical resistance using the inverse of the calibration curve. A sample figure of this procedure is shown in Figure 5.4. After calculating

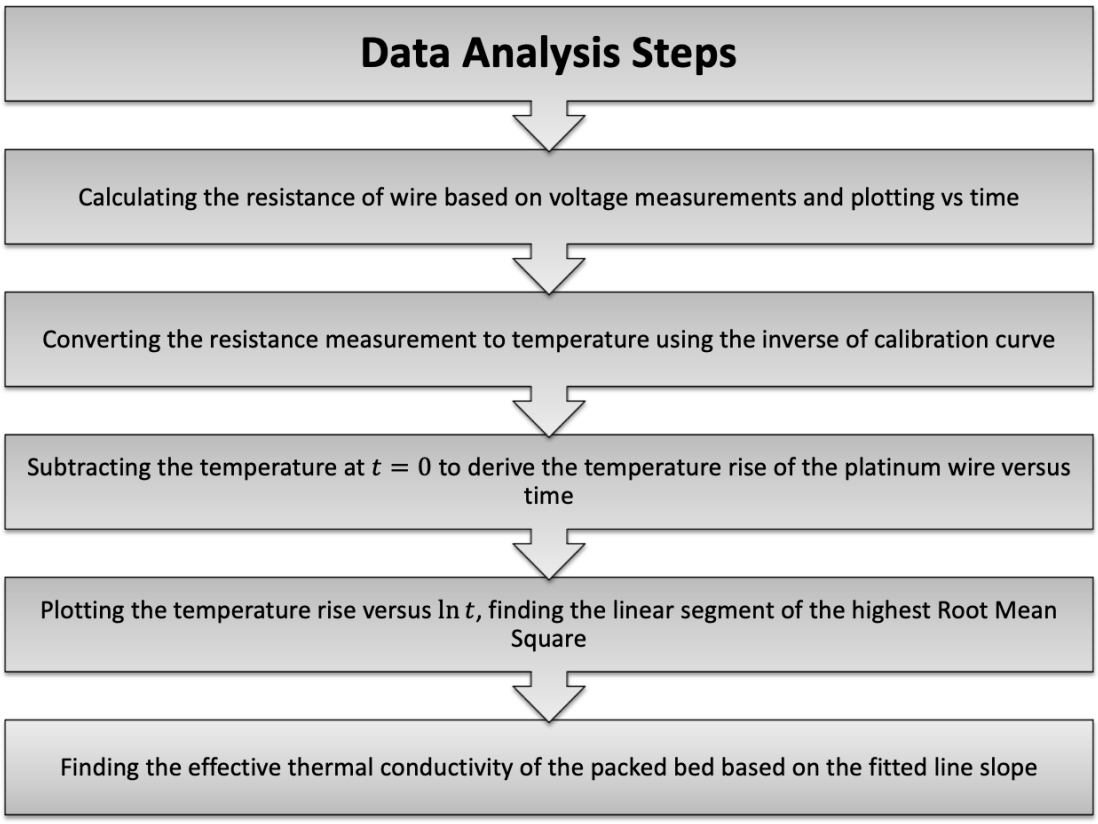

Figure 5.2: A schematic of data analysis steps to calculate the effective thermal conductivity of packed bed of magnesium-manganese-oxide pellets

the wire's temperature, the temperature rise can be derived by subtracting the temperature at $t = 0$ from wire's temperature. Then temperature rise of the platinum wire is plotted versus $\ln(t)$, and a straight line is fitted through the most linear segment of the curve. This segment was chosen by maximizing R^2 as suggested by ASTM standard [33]. Samples of these plots are shown in Figures 5.4 - 5.7. After fitting the straight line, the effective thermal conductivity of the packed bed is calculated as follows:

$$k_{\text{eff}} = \frac{Q}{4\pi m} \tag{5.2}$$

In which m is the slope of the linear curve, and Q is the power of the platinum wire per length, which can be calculated as follows:

$$Q = \frac{V_{\text{wire}} I}{l_{\text{wire}}} \tag{5.3}$$

And l_{wire} is the length of the platinum wire.

This procedure is repeated for all of the measurements in three experiments. The results are shown

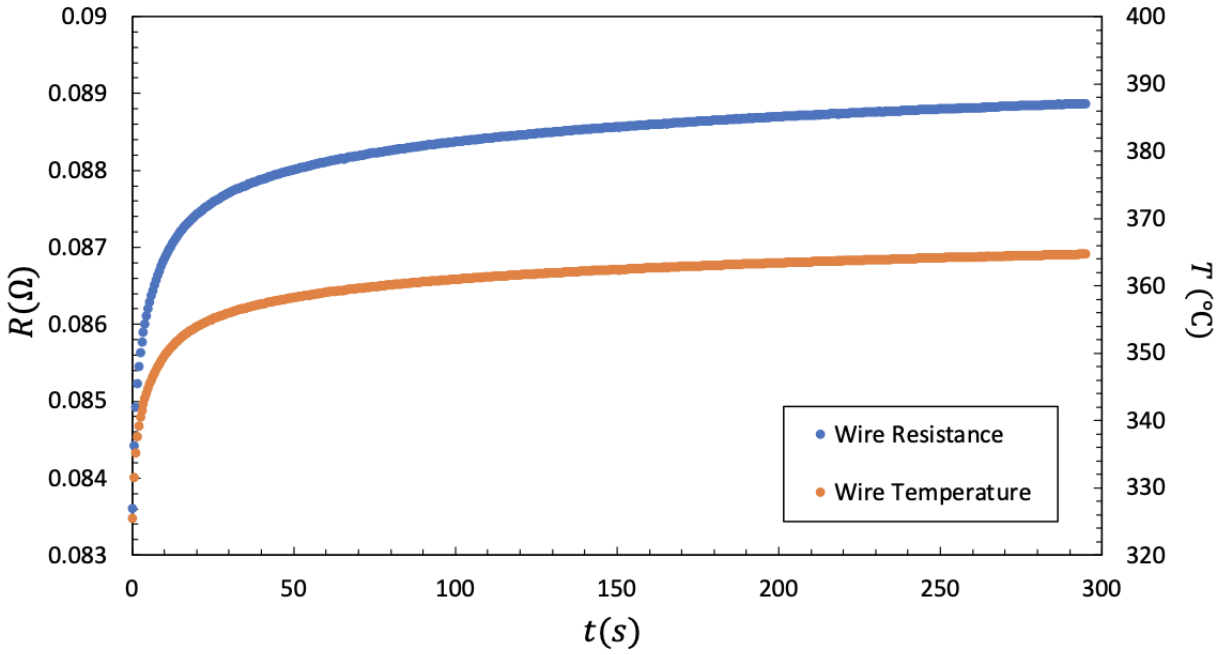

Figure 5.3: A sample plot of the platinum's wire electrical resistance and the calculated wire's temperature versus time. Experiment 3 - T = 300°C.

in Tables 5.3 - 5.5. The cells with green color have an R^2 higher than 0.9998, in which the noise level is low and have the highest level of accuracy. Two measurement in experiment 1 have an R^2 lower than 0.999, which are ruled out due to the relatively high level of noise. As shown in the Table 5.5, Experiment 3 has the highest R^2 values and R^2 and t_{start} tend to decrease with increasing temperature. The lower t_{start} in higher temperatures is consistent with the lower limit introduced by Vos [2]. As the effective thermal conductivity increases, less time is need for the material to reach thermochemical equilibrium.

5.3 Uncertainty Analysis

In this section, the effect of t_{start} on the effective thermal conductivity of the packed bed is discussed. As mentioned before, for all of the measurements, t_{start} is chosen by maximizing R^2, as suggested by ASTM standard [34], rather than the lower limit offered by Vos [2]. This is due to the

T(°C)	k_{eff}	t_{start}	R^2
312.5	0.4644	81.5	0.9990
411.6	0.5296	55.0	0.9991
509.8	0.6097	55.0	0.9965
603.8	0.7240	55.0	0.9986
704.1	0.8152	55.0	0.9991
800.1	0.8470	20.5	0.9942
898.9	0.9534	45.0	0.9974
999.0	1.0021	16.5	0.9885
1092.7	1.2033	40.5	0.9974
1190.0	1.3410	25.0	0.9961
1287.5	1.3970	33.5	0.9814

Table 5.3: Experiment 1- The effective thermal conductivity of the packed bed of magnesium-manganese oxide pellets measured in Experiment 1

T(°C)	k_{eff}	t_{start}	R^2
312.6	0.4722	73.7	0.9986
409.8	0.5536	66.8	0.9987
509.8	0.6403	60.4	0.9986
606.7	0.7483	54.6	0.9985
704.1	0.8152	33.6	0.9974
800.8	0.9415	60.5	0.9998
898.9	0.9995	54.8	0.9996
999.7	1.1113	45.0	0.9986
1097.3	1.2726	40.0	0.9995
1190.0	1.3911	33.5	0.9992
1295.2	1.4543	15.02	0.9967

Table 5.4: Experiment 2- The effective thermal conductivity of the packed bed of magnesium-manganese oxide pellets measured in Experiment 2

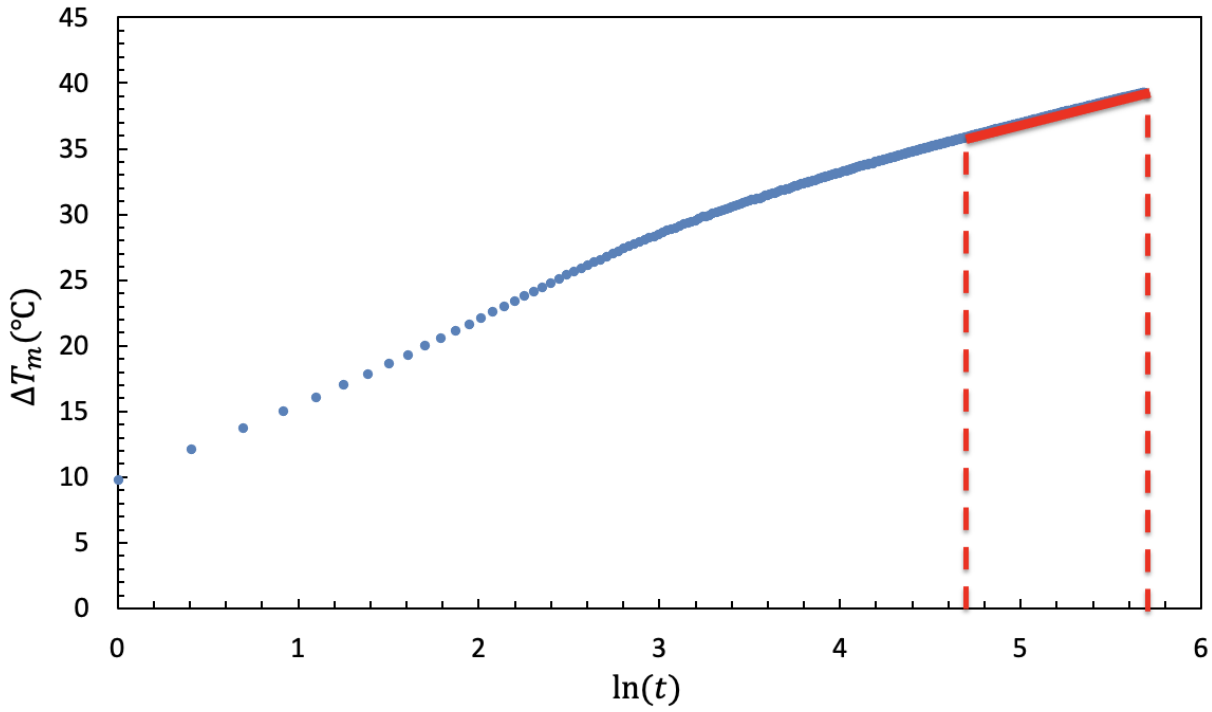

Figure 5.4: Temperature rise of the platinum wire versus ln(t). Experiment 3 - T = 300°C

non-homogeneous structure of the packed bed; as non-homogeneous materials need a longer time to reach the equilibrium state.

Two measurements from experiment one are chosen to assess the effect of t_{start} on the effective thermal conductivity of the packed. The first measurement is T = 700°C, with a maximum R^2 of 0.9991, the highest achieved R^2 in the set, and the second one is T = 800°C with an R^2 of 0.991, showing relatively high levels of noise in the measurement. The plots for these measurements are shown in Figures 5.8 - 5.11.

The effective thermal conductivity is calculated by choosing different ln (t_{start}) for these two measurements, and results are shown in Tables 5.6, and 5.7. For a better comparison, the results are plotted in Figure 5.12. The red dot indicates the highest R^2 achieved in the measurement. As shown in Figure 5.12, the effective thermal conductivity increases rapidly with increasing t_{start} before the red dot. The effective thermal conductivity still continues to increase after the red dot, but with a significantly lower rate. The error between the highest calculated thermal conductivity

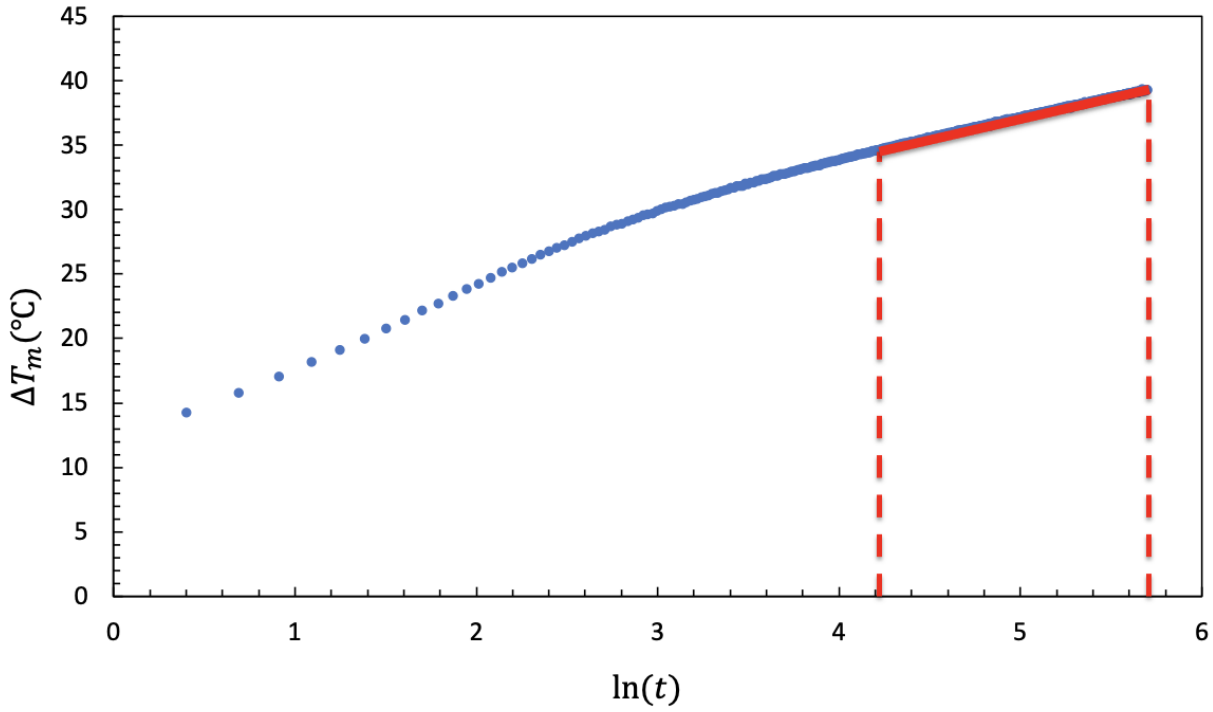

Figure 5.5: Temperature rise of the platinum wire versus ln(t). Experiment 3 - T = 600°C

and the thermal conductivity with the highest R^2 is three percent for T = 700 °C, and seven percent for T = 800 °C. The seven percent is chosen as the uncertainty level for all measurements.

Although the effective thermal conductivity converged for both cases, the noisier measurement achieved the highest R^2 at a lower t_{start} compared to the previous and subsequent temperature 5.3. Choosing the lower t_{start} results in underpredicting the effective thermal conductivity. So, it can be concluded that the noise level of measurement is crucial for accurate results. Due to this fact, the results of two measurements with R^2s below 0.99, are discarded. The results of three experiments, beside the mathematical modeling with M_{bed} = 6 is shown in Figure.

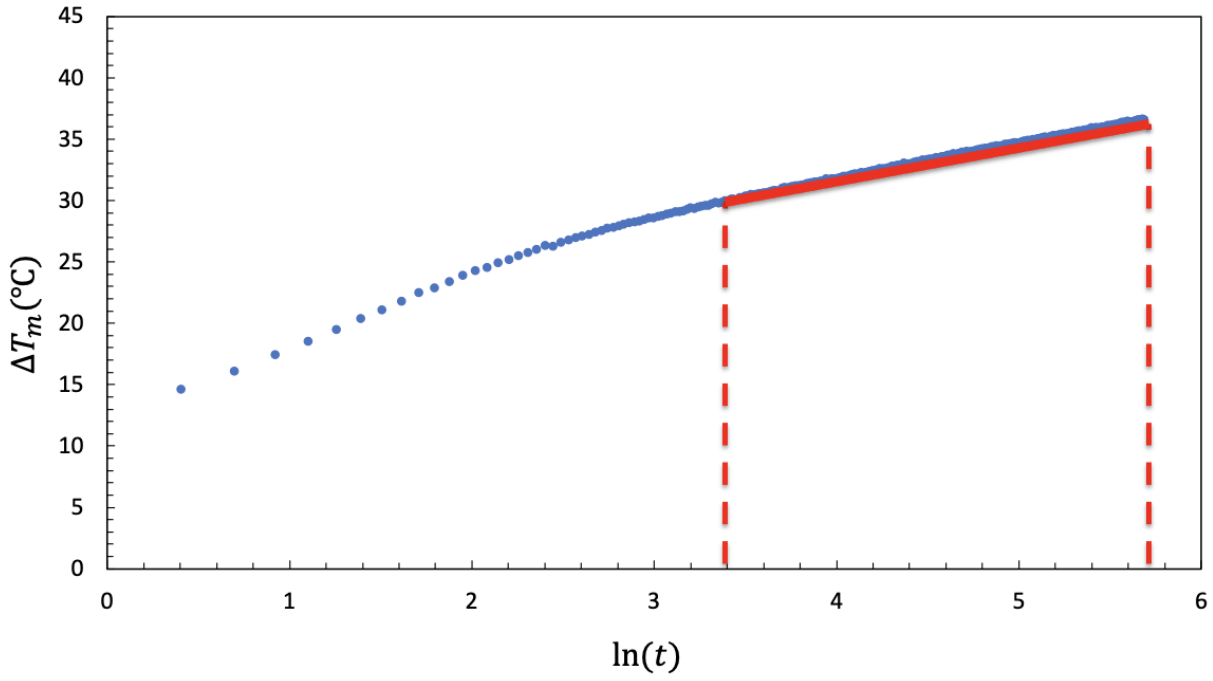

Figure 5.6: Temperature rise of the platinum wire versus ln(t). Experiment 3 - T = 1000°C

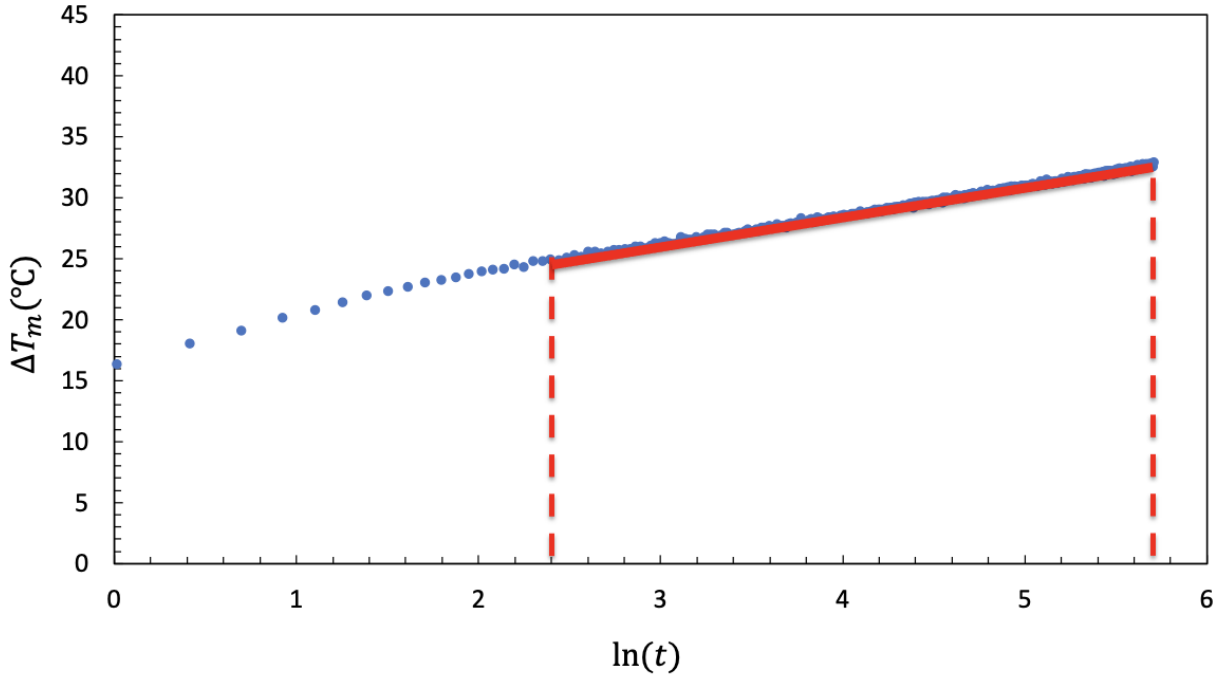

Figure 5.7: Temperature rise of the platinum wire versus ln(t). Experiment 3 - T = 1400°C

T(°C)	k_{eff}	t_{start}	R^2
310.0	0.4879	122	0.9997
410.3	0.5796	90.1	0.9996
508.7	0.6403	81.5	0.9996
606.6	0.7589	67.0	0.9994
704.3	0.8707	60.5	0.9995
799.7	0.9534	49.5	0.9993
898.7	0.9988	33.5	0.9993
999.6	1.1302	30.0	0.9988
1097.6	1.1934	25.0	0.9995
1195.9	1.3663	22.5	0.9988
1294.6	1.5172	18.5	0.9978
1394.0	1.6430	11.5	0.9970

Table 5.5: Experiment 3- The effective thermal conductivity of the packed bed of magnesium-manganese oxide pellets measured in Experiment 3

$\ln(t_{start})$	$t_{start}(s)$	k_{eff}	R^2
0.6935	2.0	0.6394	0.9608
1.0986	3.0	0.6556	0.9657
1.5041	4.5	0.6769	0.9729
2.0149	7.5	0.7098	0.9836
2.5257	12.5	0.7447	0.9922
3.0204	20.5	0.7747	0.9966
3.5116	33.5	0.7996	0.9986
4.0073	55.0	0.8188	0.9991
4.5034	90.5	0.8307	0.9986
5.0006	148.5	0.8406	0.9962
5.5013	245.0	0.8461	0.9550

Table 5.6: The effective thermal conductivity of the packed bed of magnesium-manganese-oxide pellets for different t_{start} - Experiment 1 - T = 700°C

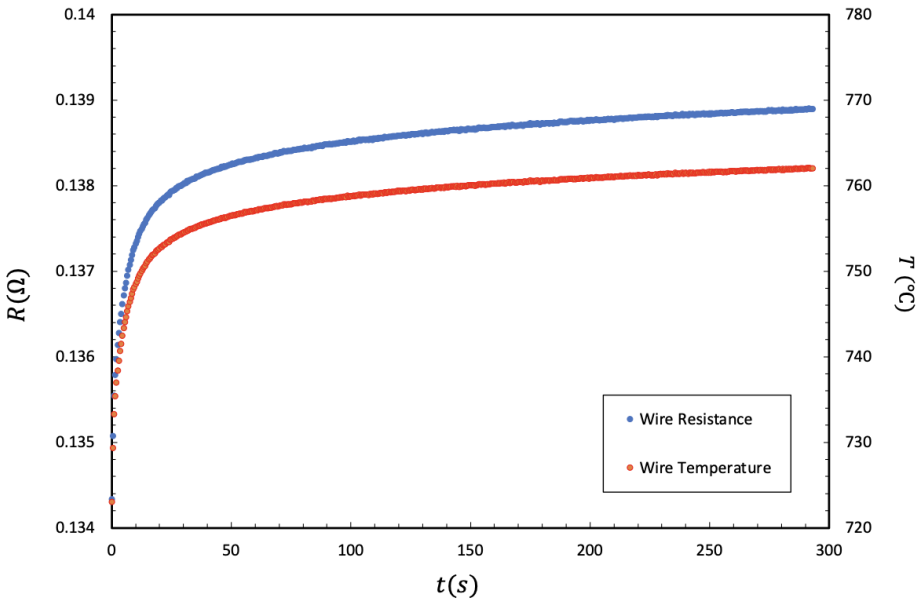

Figure 5.8: The temperature rise of the platinum wire versus $\ln(t)$ - Experiment 1 - T = 700°C with an R^2 of 0.9991, the highest achieved R^2 in the experiment set.

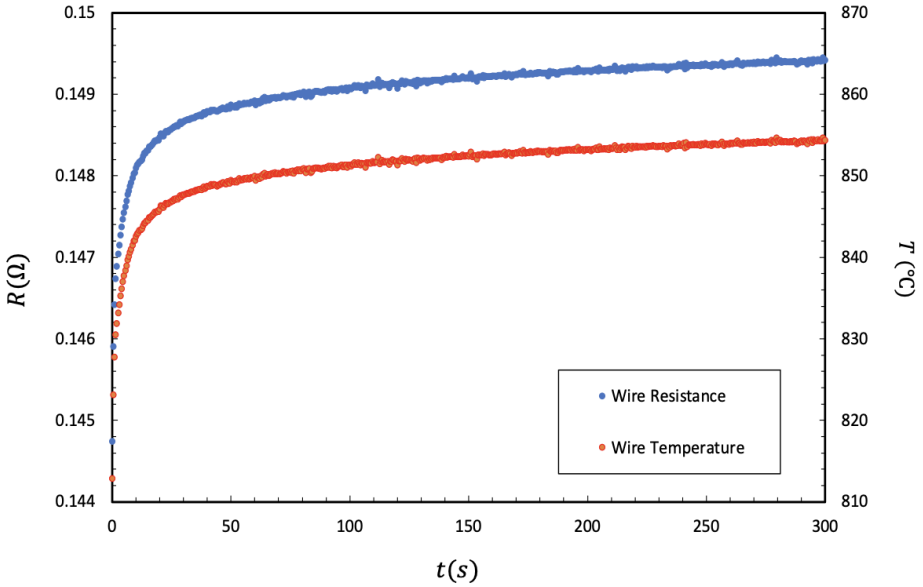

Figure 5.9: The temperature rise of the platinum wire versus $\ln(t)$ - Experiment 1 - T = 800°C with an R^2 of 0.9940, one the lowest achieved R^2 in the experiment set.

$\ln(t_{start})$	$t_{start}(s)$	k_{eff}	R^2
0.6932	2.0	0.6974	0.9605
1.0986	3.0	0.7163	0.9659
1.5041	4.5	0.7410	0.9737
2.0149	7.5	0.7777	0.9842
2.5257	12.5	0.8135	0.9907
3.0204	20.5	0.8470	0.9942
3.5116	33.5	0.8691	0.9938
4.0073	55.0	0.8813	0.9900
4.5034	90.5	0.8952	0.9805
5.0006	148.5	0.9061	0.9492
5.5013	245.0	0.8733	0.4359

Table 5.7: The effective thermal conductivity of the packed bed of magnesium-manganese-oxide pellets for different t_{start} - Experiment 1 - T = 800°C

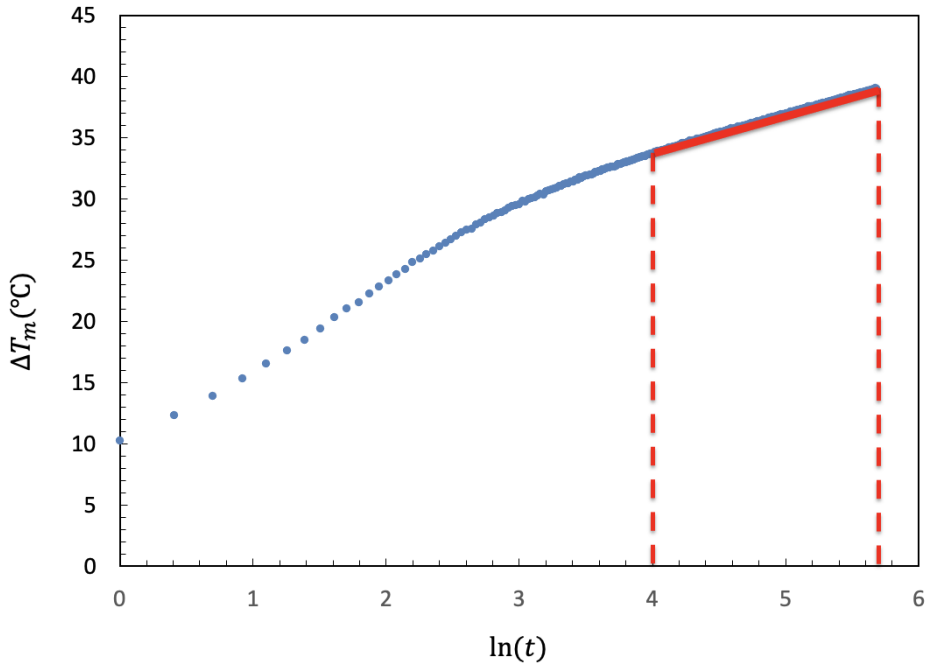

Figure 5.10: The temperature rise of the platinum wire versus ln t - Experiment 1 - T = 700°C

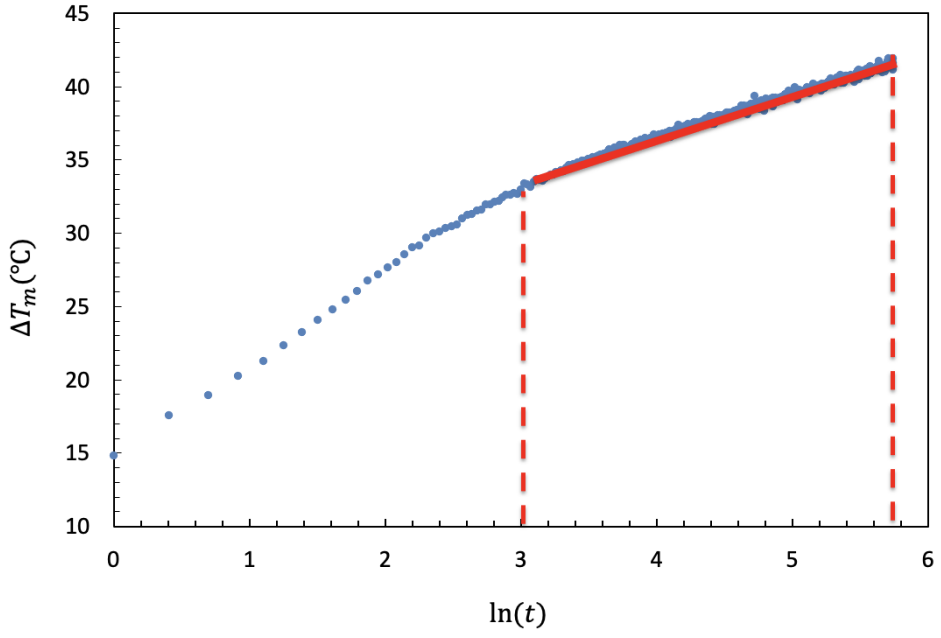

Figure 5.11: The temperature rise of the platinum wire versus ln t - Experiment 1 - T = 800°C

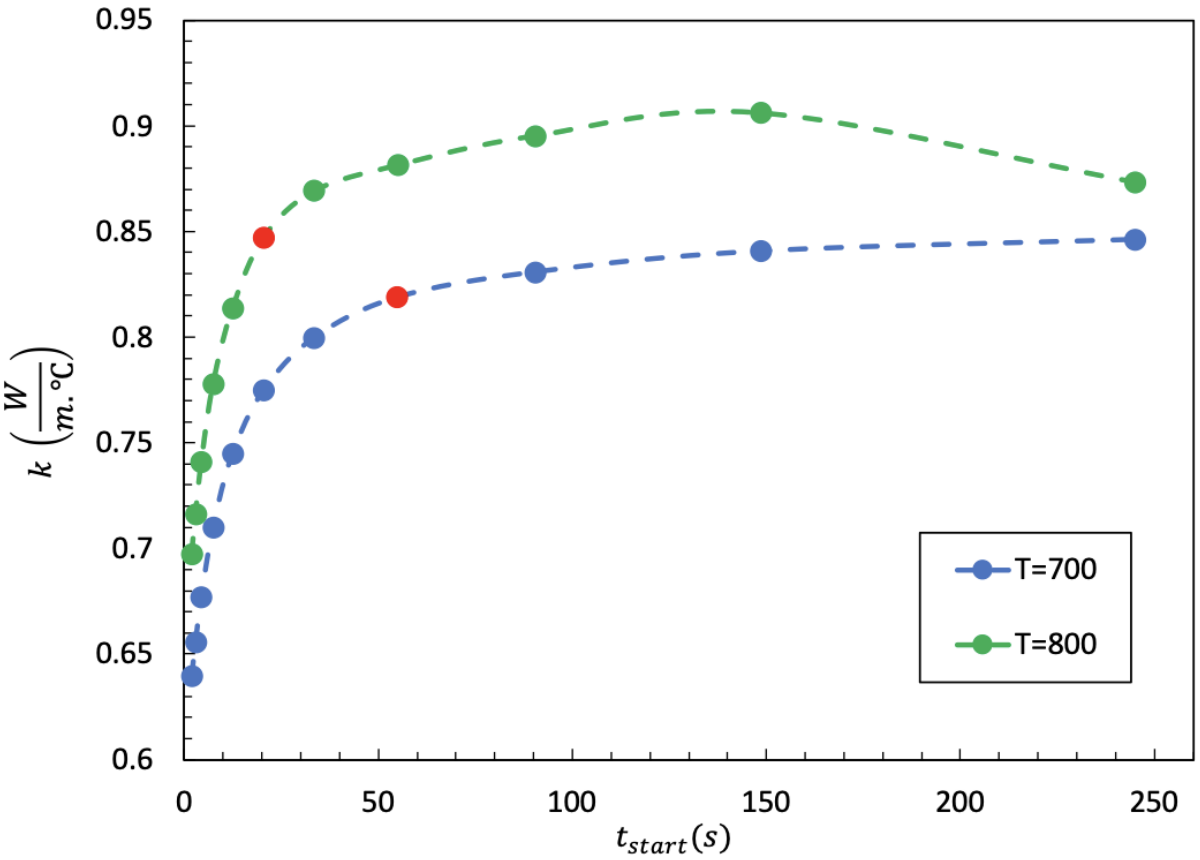

Figure 5.12: The effect of t_{start} on calculation of the effective thermal conductivity of the packed bed at T = 700 °C and T = 800 °C - Experiment 1

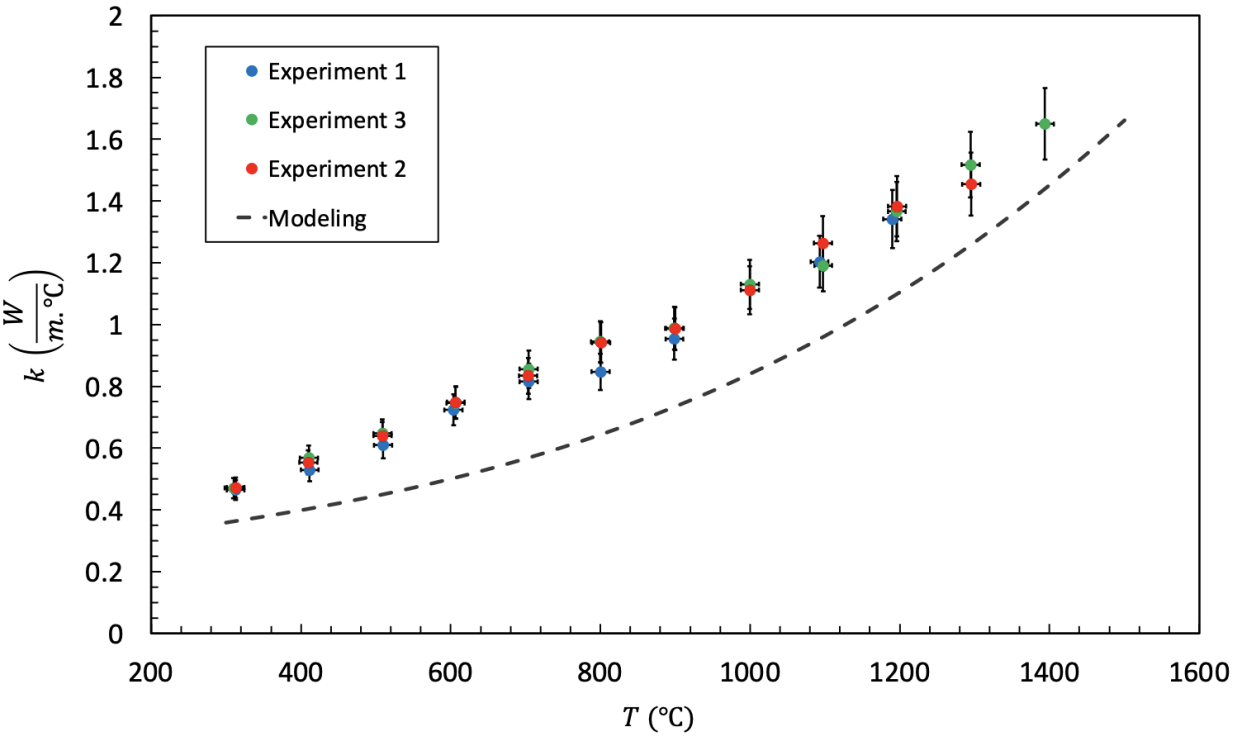

Figure 5.13: The effective thermal conductivity of the packed bed of magnesium-manganese-oxide pellets measured by a modified transient hot-probe method: Experiments are done in three sets to ensure the repeatability of measurements. The experimental results are compared to the theoretical modeling, and the result shows the best agreement when $M_{\text{bed}} = 6$.

CHAPTER 6

CONCLUSION

In this thesis, a modified transient hot-wire method is used to determine the effective thermal conductivity of the packed bed of magnesium-manganese-oxide pellets at various temperatures (300-1400 °C with 100 °C intervals). The modified transient hot-wire is a simple and effective method to measure effective thermal conductivity at higher temperatures. This method predicts the thermal conductivity based on the linear segment of the temperature rise versus $\ln(t)$. The experimental results show the effective thermal conductivity of the packed bed is strongly dependent on the temperature, increasing from 0.45 to 1.64 $\left(\frac{W}{m^{\circ}C}\right)$ in temperatures 300 to 1400 °C. This increase in the effective thermal conductivity is primarily attributed to radiation. Experiments are conducted in three sets to ensure repeatability, and the results of the three experiments were consistent with each other.

Even though this method is mathematically simple, it is highly sensitive to the data noise level. Experiments with a higher level of noise ($R^2 < 0.998$) can result in underpredicting the effective thermal conductivity, so having the highest level of accuracy in measurements is crucial for this technique. The uncertainty is calculated by choosing different portions of the $\Delta T - \ln(t)$ curve to estimate the effective thermal conductivity.

The experimental results are compared to a dual-porosity model, estimating the effective thermal conductivity at small-scale (magnesium-manganese-oxide pellet) and large-scale (packed bed). The theoretical model consists of two terms, conduction and radiation. Krupiczka model is used for the conduction component of the packed bed. The radiation component is estimated based on the Rosseland diffusion approximation, using different extinction coefficients. The rate of increase in the effective thermal conductivity of the packed bed is best matched when $M_{\text{bed}} = 6$, which is a coefficient in the extinction coefficient offered by Hsu and Howel [23]. The dual-porosity model predicts lower values of the packed bed's effective thermal conductivity compared to experimental results. The underprediction can be due to several model assumptions. For example, the

thermal conductivity of magnesium-manganese-oxide is estimated by a mixing model, while we know magnesium-oxide and manganese-oxide chemically bond and form new compounds, such as perovskites, during the solid mixing process. Furthermore, the thermal conductivity of manganese-oxide has to be extrapolated for temperatures above 800 °C due to the lack of experimental data, which may introduce errors for higher temperatures. Due to these shortcomings of theoretical modeling, the experimental measurements are needed.

BIBLIOGRAPHY

BIBLIOGRAPHY

[1] Y. S. Touloukian. *Thermal conductivity: nonmetallic solids [by] Y. S. Touloukian [and others]*. IFI/Plenum New York, 1970.

[2] Vos. B. H. Measurements of thermal conductivity by a non-steady-state method. *Applied Scientific Research, Section A*, 5:425–438, 1956.

[3] Jaume Cot-Gores, Albert Castell, and Luisa F. Cabeza. Thermochemical energy storage and conversion: A-state-of-the-art review of the experimental research under practical conditions. *Renewable and Sustainable Energy Reviews*, 16(7):5207–5224, 2012.

[4] J. Sunku Prasad, P. Muthukumar, Fenil Desai, Dipankar N. Basu, and Muhammad M. Rahman. A critical review of high-temperature reversible thermochemical energy storage systems. *Applied Energy*, 254:113733, 2019.

[5] Kelvin Randhir, Keith King, Nathan Rhodes, Like Li, David Hahn, Renwei Mei, Nicholas AuYeung, and James Klausner. Magnesium-manganese oxides for high temperature thermochemical energy storage. *Journal of Energy Storage*, 21:599 – 610, 2019.

[6] Keith King, Kelvin Randhir, Joerg Petrasch, and James Klausner. Enhancing thermochemical energy storage density of magnesium-manganese oxides. *Energy Storage*, 1(5):e83, 2019.

[7] Kelvin Randhir, Keith King, Joerg Petrasch, and James Klausner. Oxidation kinetics of magnesium-manganese oxides for high-temperature thermochemical energy storage. *Energy Technology*, 8(10):2000063, 2020.

[8] Christopher Kang, Yi-Hyun Park, Jon T. Van Lew, Alice Ying, Mohamed Abdou, and Seungyon Cho. Transient hot-wire experimental system for measuring the effective thermal conductivity of a ceramic breeder pebble bed. *Fusion Science and Technology*, 72(3):263–270, 2017.

[9] D. Kraemer and G. Chen. A simple differential steady-state method to measure the thermal conductivity of solid bulk materials with high accuracy. *Review of Scientific Instruments*, 85(2):025108, 2014.

[10] Wendi Guo, Jim Lim, Xiaotao Bi, Shahab Sokhansanj, and Staffan Melin. Determination of effective thermal conductivity and specific heat capacity of wood pellets. *Fuel*, 103:347–355, 01 2013.

[11] G Piazza, M Enoeda, and A Ying. Measurements of effective thermal conductivity of ceramic breeder pebble beds. *Fusion Engineering and Design*, 58-59:661–666, 2001.

[12] Jean Côté and Jean-Marie Konrad. Assessment of structure effects on the thermal conductivity of two-phase porous geomaterials. *International Journal of Heat and Mass Transfer*, 52(3):796 – 804, 2009.

[13] M. Enoeda, K. Furuya, H. Takatsu, S. Kikuchi, and T. Hatano. Effective thermal conductivity measurements of the binary pebble beds by hot wire method for the breeding blanket. *Fusion Technology*, 34:877–881, 1998.

[14] Hans-Peter Ebert, V. Bock, O. Nilsson, and J. Fricke. The hot-wire method applied to porous materials of low thermal conductivity. *High Temp.-High Press.*, 25:391–402, 01 1993.

[15] B. Pilkington. In situ measurements of building materials using a thermal probe. 2008.

[16] Laurent Marmoret and Hussein Humaish. Limit of validity of the log-linear model for determining thermal properties of light insulation materials with cylindrical hot probe. *International Journal of Thermal Sciences*, 117:251 – 259, 2017.

[17] ARTHUR L. LOEB. Thermal conductivity: Viii, a theory of thermal conductivity of porous materials. *Journal of the American Ceramic Society*, 37(2):96–99, 1954.

[18] I.H. Tavman. Effective thermal conductivity of granular porous materials. *International Communications in Heat and Mass Transfer*, 23(2):169–176, 1996.

[19] M. Quintard. Introduction to heat and mass transport in porous media. 2016.

[20] James Clerk Maxwell. *SPHERICAL HARMONICS*, volume 1 of *Cambridge Library Collection - Physical Sciences*, page 157–180. Cambridge University Press, 2010.

[21] T. J. Hendricks and J. R. Howell. Absorption/Scattering Coefficients and Scattering Phase Functions in Reticulated Porous Ceramics. *Journal of Heat Transfer*, 118(1):79–87, 02 1996.

[22] J.R. Howell, M.P. Menguc, and R. Siegel. *Thermal Radiation Heat Transfer, 5th Edition*. CRC Press, 2010.

[23] Pei feng Hsu and John R. Howell. Measurements of thermal conductivity and optical properties of porous partially stabilized zirconia. *Experimental Heat Transfer*, 5(4):293–313, 1992.

[24] Lisa-Marie Heisig, Katrin Markuske, Eric Werzner, Rhena Wulf, and Tobias M. Fieback. Experimental and simplified predictive determination of extinction coefficients of ceramic open-cell foams used for metal melt filtration. *Advanced Engineering Materials*, n/a(n/a):2100723.

[25] Fritz Zaversky, Leticia Aldaz, Marcelino Sánchez, Antonio L. Ávila Marín, M. Isabel Roldán, Jesús Fernández-Reche, Alexander Füssel, Wieland Beckert, and Jörg Adler. Numerical and experimental evaluation and optimization of ceramic foam as solar absorber – single-layer vs multi-layer configurations. *Applied Energy*, 210:351–375, 2018.

[26] Anabel Palacios, Lin Cong, M.E. Navarro, Yulong Ding, and Camila Barreneche. Thermal conductivity measurement techniques for characterizing thermal energy storage materials – a review. *Renewable and Sustainable Energy Reviews*, 108:32–52, 2019.

[27] E.F.M. Van Der Held, J. Hardebol, and J. Kalshoven. On the measurement of the thermal conductivity of liouids by a non-stationary method. *Physica*, 19(1):203 – 216, 1953.

[28] E.F.M. Van Der Held and F.G. Van Drunen. A method of measuring the thermal conductivity of liquids. *Physica*, 15(10):865 – 881, 1949.

[29] J. Blackwell. A transient-flow method for determination of thermal constants of insulating materials in bulk part i—theory. *Journal of Applied Physics*, 25:137–144, 1954.

[30] J. H. Blackwell. The axial-flow error in the thermal-conductivity probe. *Canadian Journal of Physics*, 34(4):412–417, 1956.

[31] Jaeger JC. Conduction of heat in an infinite region bounded internally by a circular cylinder of a perfect conductor. *Australian Journal of Physics*, 9(2):167–179, 1956.

[32] Da de Vries and Aj Peck. On the cylindrical probe method of measuring thermal conductivity with special reference to soils. i. extension of theory and discussion of probe characteristics. *Australian Journal of Physics*, 11:255–271, 1958.

[33] ASTM D5334-14. Standard test method for determination of thermal conductivity of soil and soft rock by thermal needle probe procedure. *ASTM International*, 2014.

[34] Standard test method for thermal conductivity of refractories by hot wire (platinum resistance thermometer technique). Standard, ASTM International, West Conshohocken,PA, 2019.

[35] http://sentrotech.wpengine.com/wp-content/uploads/2016/08/stt-1600c-12tube-data-sheet.docx.

[36] https://labjack.com/support/software/applications/t-series/kipling.

[37] John Arblaster. Selected electrical resistivity values for the platinum group of metals part i: Palladium and platinum. *Johnson Matthey Technology Review*, 59:174–181, 07 2015.